MDPI

Numerical Analysis of the Effects of Different Rotor Tip Gaps in a Radial Turbine Operating at High Pressure Ratios Reaching Choked Flow

José Galindo [1], Andrés Tiseira [1], Roberto Navarro [1], Lukas Benjamin Inhestern [2] and Juan David Echavarría [1,*]

[1] CMT-Motores Térmicos, Universitat Politècnica de València, Camino de Vera s/n, 46022 Valencia, Spain
[2] Institut für Luft-und Raumfahrt, Technische Universität Berlin, Marchstraße 12/14, 10587 Berlin, Germany
* Correspondence: juaecol@mot.upv.es; Tel.: +34-963877650

Abstract: To operate, radial turbines used in turbochargers require a minimum tip gap between the rotor blades and the stationary wall casing (shroud). This gap generates leakage flow driven by the pressure difference between the pressure and suction side. The tip leakage flow is largely unturned, which translates into a reduction of the shaft work due to the decrease in the total pressure. This paper investigates the flow through the rotor blade tip gap and the effects on the main flow when the turbine operates at a lower and higher pressure ratio with the presence of supersonic regions at the rotor trailing edge for two rotational speeds using computational fluid dynamics (CFD). The rotor tip gap has been decreased and increased up to 50% of the original tip gap geometry given by the manufacturer. Depending on the operational point, the results reveal that a reduction of 50% of the tip gap can lead to an increase of almost 3% in the efficiency, whereas a rise in 50% in the gap penalty the efficiency up to 3%. Furthermore, a supersonic region appears in the tip gap just when the flow enters through the pressure side, then the flow accelerates, leaving the suction side with a higher relative Mach number, generating a vortex by mixing with the mainstream. The effects of the vortex with the variation of the tip gap on the choked area at the rotor trailing edge presents a more significant change at higher than lower speeds. At a higher speed, the choked region closer to the shroud is due to the high relative inlet flow angle and the effects of the high relative motion of the shroud wall. Furthermore, this relative motion forces the tip leakage vortex to stay closer to the tip suction side, generating a subsonic region, which increases with the tip gap height. The leakage flow at lower and higher rotational speed does not affect the main flow close to the hub. However, close to the shroud, the velocity profile changes, and the generated entropy increases when the flow goes through the tip gap.

Keywords: choked flow; sonic conditions; CFD; tip gap; tip leakage; scraping flow; pressure profile

1. Introduction

Radial turbines are widely used in the transport industry. They are part of the super-charging system of engines used for various actions in different branches of the transport industry such as air, land, and water transport [1,2] in fossil fuel engines [3] as well as in hydrogen hybrid engines [4–6], hybrid electrical turbines [7], fuel cells [8], biofuel propulsion [9,10], and Organic Rankine Cycle [11–13]. Therefore, the improvement of the radial turbine in these systems still plays an important role in the current propulsion technologies.

Over the last few years, with the improvement of computational tools and experimental measuring techniques, different studies have been carried out to characterize the internal flow behavior of the radial turbine as the flow goes through its components such as the volute, stator, and rotor. However, since radial turbine geometry is quite compact and relatively small, especially in urban automotive engines, the installation of sensors in each of the aforementioned elements is quite limited [14] and in some cases it is necessary

to scale the geometry [15,16] to measure the pressure and velocity inside the stator [17]. Furthermore, the complex three-dimensional flow structure occurring in the stage turbine cannot be completely modeled by the one-dimensional approach available in the literature [18]. Thus, the use 3D computational fluid dynamics (CFD) stands as an important tool to analyze losses , improve turbine internal aerodynamic performance [19], and the development of one-dimensional models to achieve a high reliability.

One of the main fluid-flow losses in a turbine corresponds to the leakage flow, i.e., secondary flows going through the narrow clearance between either the impeller or the stator vanes and the turbine housing. Nevertheless, due to the increasing interest in renewable energy sources as hydropower, where mechanical systems such as pumps and reverse-operated pumps can be found, the presence of tip leakage flow can produce vortical flow structures leading to considerable pressure losses and cavitation problems [20–23]. Using CFD, Tamaki et al. [14] found that the leakage flow in the stator increases as the nozzle opening decreases; besides, the existence of the nozzle clearance is a factor that decreases the turbocharger performance during the period of the engine acceleration. Moreover, the study of Zhao et al. [24] showed that the increase in the endwall clearance leads to a significant rise in the Mach number throughout the chord due to the reduction of the boundary layer effects in this region and can decrease the spanwise height of shock waves at the nozzle exit. Regarding rotor leakage flow, the study of He et al. [25] disclosed that among tip clearance, backface clearance, and backface cavity (all three in the rotor), the tip clearance flow (also known as tip leakage) has the most significant impact on the aerodynamic parameters at the rotor outlet, and the maximum efficiency penalty is about 7.7%.

With the intention to propose one-dimensional loss models and design procedures in radial turbine, several numerical studies have been focused on the impact of blade loading on rotor tip leakage, as often a higher blade loading causes greater tip leakage, which in turn decreases turbine efficiency [26,27]. However, Zhang et al. [28] show that, in a high pressure turbine, the local flow through the tip gap may choke, therefore limiting the effect of blade loading over tip leakage mass flow rate. In a similar study using CFD, Wheeler et al. [29] showed that, as the blade exit Mach number is increased, the tip leakage flow becomes choked and invariant to changes in the flow through the blade, thus reducing the tip losses.

Other studies have presented experimental and numerical investigations not only of the aerodynamic conditions but also of aerothermal performance [30] of an uncooled winglet tip, under transonic conditions, as by O'Dowds et al. [31]. The results reveal that the local heat transfer distribution on the rotor blade tip is affected by the relative casing motion and leads to a smaller supersonic region over the tip. However, a significant portion of the tip leakage flow remains transonic with identifiable choked regions and shock wave structures. It is worth mentioning that most studies related to turbine tip leakage corresponds to axial configurations rather than radial turbines as well as when comparing the leakages losses in axial and radial turbines [32,33]. For the analysis of radial turbine leakage flow, we highlight the experimental work of Dambach et al. [34] and the CFD and loss model of Serrano et al. [35].

The objective of this study is to gain more insight into tip leakage flow behavior in radial turbines at high pressure ratios reaching choked flow. We analyze the interactions with the main flow through the rotor and whether the tip leakage is responsible for the subsonic regions at rotor TE at a low rotational speed, besides the impact on the turbine efficiency [36]. By addressing these issues, the current study provides a better understanding of the tip leakage loss mechanisms, introducing design guidelines for manufacturers to improve their tip clearance profiles and suggesting to researchers how to enhance their one-dimensional loss models. These models are commonly based on correlations with the rotational speed and blade loading, and for the case of a VGT system, an equivalent nozzle is evaluated [37]. The model is fed some experimental points under normal operational conditions rather than at off-design conditions as higher pressure ratios. Thus, when the

flow dynamic through the tip gap approaches the choked conditions presented in this work it adds information to the development of one-dimensional models in future works.

The current work is divided into four sections. The Section 2 presents the geometry description of the radial turbine, followed by the numerical model and methods implemented in the Section 3. In the Section 4, the results and analysis of the numerical simulation are presented, explaining the performance characteristics of the selected operational points, the effects of tip leakage on the rotor blade, and the impact of varying the tip gap on the main flow. Finally, the conclusions of the obtained results form the Section 5 of this paper.

2. Geometry Description

A variable geometry turbocharger turbine (also known as variable-nozzle turbine) used in a commercial automotive diesel engine of 2 L has been considered for this study. Three variations in the geometry of the rotor tip gap are presented, as shown in Figure 1, corresponding to a decrease in the gap with respect to the original geometry of 25% and 50%. These cases will be denoted as -25 pTG and -50 pTG, respectively. The third case corresponds to an increase in the gap of 50% and will be denoted as +50 pTG. The tip gap of the original geometry given by the manufacturer will be denoted as +0 pTG. Figure 2 depicts the geometry of the rotor and stator. The rotor owns 9 blades, while the stator has 11 vanes. The same stator vanes position is used for all the cases: a blade angle α equal to 53.45° represents an 80% VGT opening, in order to obtain the choked flow at the rotor outlet. Table 1 provides geometrical information about the employed turbine. The computational fluid domain illustrated in Figure 3 consists of the inlet and outlet ducts, the volute, stator, and rotor. The inlet duct has a length of 200 mm (6 times the inlet duct diameter) and the outlet duct has a length 400 mm (9 times the outlet duct diameter). The virtual measuring sections in the inlet and outlet duct are located at the same position of the corresponding experimental probes, which are located according to the turbocharger gas stand test code [38]. A convergent duct with an exit diameter equal to the rotor outlet diameter is placed downstream of the outlet probe section. The convergent duct is used to achieve a similar static pressure in the outlet of the domain as expected in the rotor outlet [39].
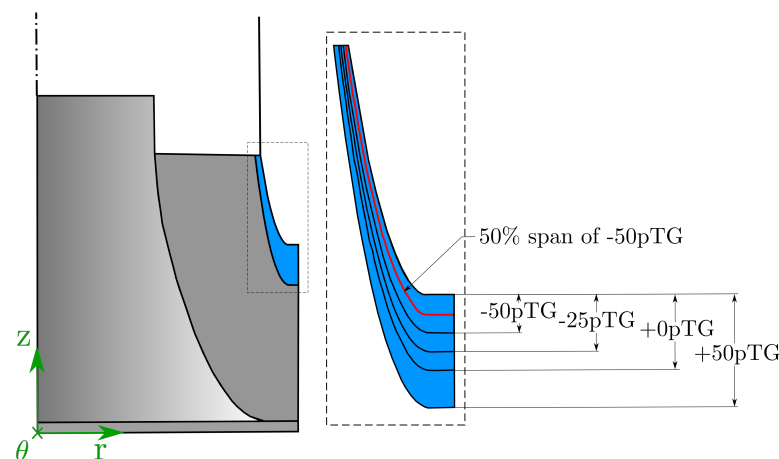

Figure 1. Geometry of the different tip gaps for the following analysis. Red line: Meridional line at 50% span of the case of -50 pTG.
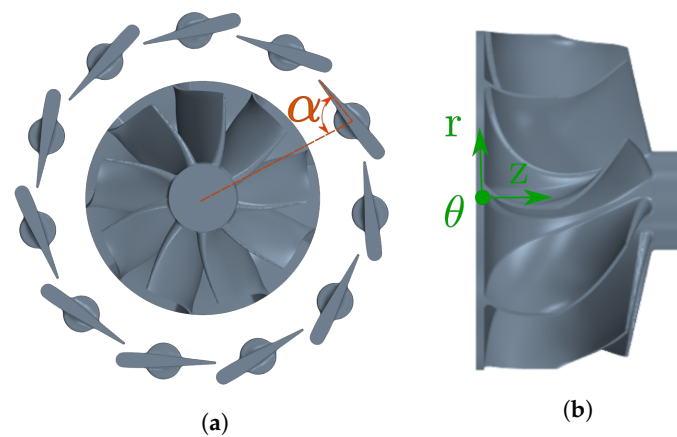
Figure 2. Turbocharger geometry. (**a**) Top view of the stator vanes and rotor; (**b**) Lateral view of the rotor.

Table 1. Turbine geometry description.

	Stator	**Rotor**			
Blade number	11	9			
Inlet diameter	-	41 mm			
Outlet diameter	-	38 mm			
Nozzle vane height	8 mm	-			
Chord length	18.95 mm	-			
Blade angle α (VGT opening)	53.45° (80%)	-			
Outlet blade angle	-	59°			
Case	-	+0 pTG	−50 pTG	−25 pTG	+50 pTG
Tip gap	0.2 mm	0.36–0.40 mm	0.18–0.20 mm	0.27–0.30 mm	0.54–0.60 mm

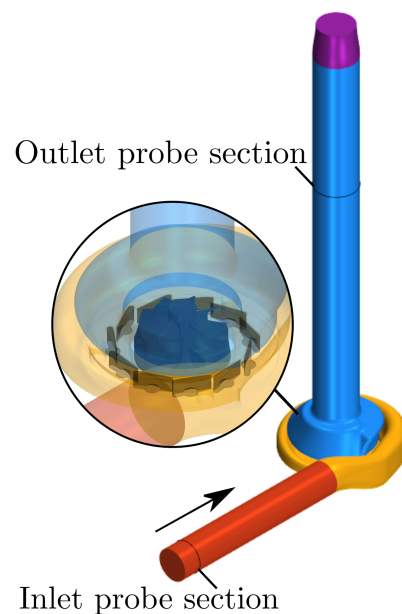**Figure 3.** Computational domain.

3. Numerical Model

The turbine selected for this study was previously modeled and tested experimentally at different conditions up to low mass flows and even negative turbine power output by Serrano et al. [27,35,39]. In the current study, the tip leakage flow and the supersonic conditions in different operational points are analyzed using the CFD software Star-CCM+

2021.1.1 (Build 16.02.009-R8). The working fluid is air and it is assumed as ideal and compressible gas. The density-based coupled solver is selected [29,40] to calculate the subsonic and supersonic conditions developed in the selected operational points. Furthermore, for the coupled flow model, the Weiss–Smith preconditioned Roe's Flux Difference Splitting (ROE FDS) scheme is selected for evaluating inviscid fluxes. The computational domain is solved using two models, steady Reynolds-averaged Navier–Stokes (RANS) considering a frozen rotor and mixing plane interfaces, as well as unsteady Reynolds-averaged Navier–Stokes (URANS). In order to determine the turbulent eddy viscosity, the turbulence model k-ω SST model [41] is chosen with compressibility correction and Durbin scale limiter for realizability. The k-ω SST model is widely recommended, and well-validated for radial turbomachinery in the literature [42–46] under subsonic, transonic, and supersonic conditions [47–49]. The SST model has seen relatively wide application in the aerospace industry, where viscous flows are typically resolved, and turbulence models are applied throughout the boundary layer. A mesh independence study was carried out in a previous study [36] to ensure valid results, as depicted in Figure 4, where a closed (10% VGT) and opened (80% VGT) position of the vanes were considered. Besides the analysis presented in this figure, where the medium core mesh represents a good option, the grid convergence index (GCI) [50] is calculated using the medium and finest mesh to quantify the numerical uncertainty, as shown in Table 2. The GCI is defined in Equation (1), where ϵ, r, and p represent the relative error between two grids, the refinement factor ratio, and the order of accuracy method, respectively. The mesh denoted as a medium core mesh with 15 cells in the boundary layer is the one selected for this study. It presents a lower GCI, implying a lower error in the mass flow rate and turbine power, which ensures the accuracy of the simulation and a grid-independent solution. The selected mesh owns 5.4 million cells and the expansion ratio in the prism layer mesh is 1.3. The inner volume of the volute, stator, and rotor has been discretized by means of an unstructured polyhedral mesh, whereas for the inlet and outlet duct, a generalized cylinder mesher has been used to generate an extruded mesh along the ducts length, as can be seen in the Figure 5. The numerical simulations are carried out with 80% VGT opening and two reduced speeds, 3882 rpm/$\sqrt{K}$ and 8421 rpm/$\sqrt{K}$, which will be designated hereinafter as the lower and the higher speeds, respectively. These rotational speeds are selected based on two aspects. First, the study of Tiseira et al. [36] used these speeds to analyze the development of sonic conditions at the stator and rotor. Second, auto-motive turbocharger turbines can reach these speeds under specific engine operating conditions as tip-in and full-load working points [51]. An inlet total pressure sweep is performed for each iso-speed line using RANS simulations until developing choke conditions. Two operational points of each speed line are solved using URANS to consider the effects of the rotor movement on the flow characteristics. These points have a total inlet pressure of 3.0 bar and 5.5 bar imposed at the inlet duct, whose corresponding pressure ratios will be labeled as the lower and the higher pressure ratio, respectively. The outlet pressure at the outlet duct has a value of 1 bar. The total inlet temperature set as a boundary condition is relatively low, 340.55 K, and the walls are considered adiabatic in accordance with previous numerical and experimental tests [36,52]. A summary of the boundary conditions values are presented in Table 3. Furthermore, it is important to remark that modifications of the tip profile as a consequence of the thermal and rotational deformation of the rotor blade [53] are not considered in the study.

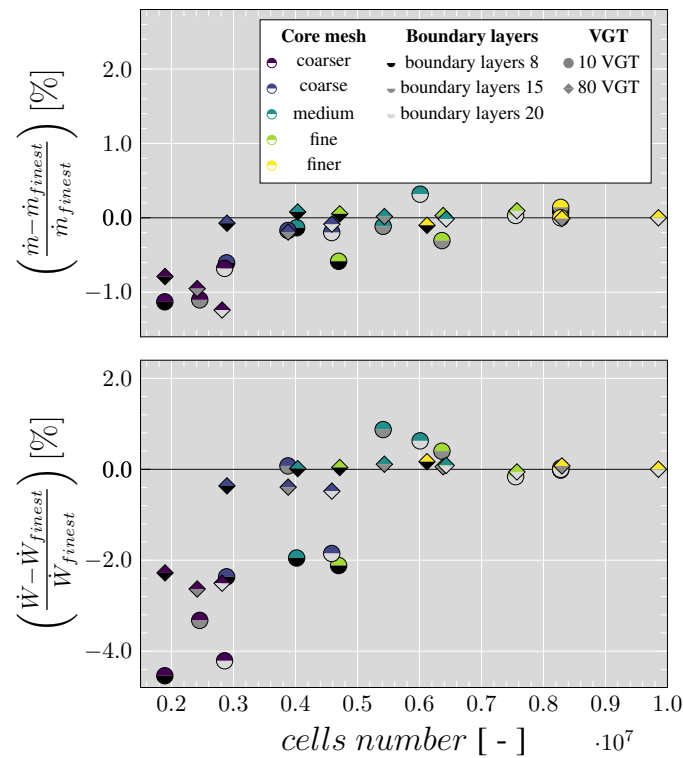$$GCI = \frac{3 \cdot |\epsilon|}{r^p - 1} \tag{1}$$

Figure 4. Variation of mass flow and turbine power with different mesh configurations relative to the finest simulated mesh for the opened and closed positions.

Table 2. Mesh independence study.

VGT [%]	Core Mesh	Boundary Layer	Cells Number [$\cdot 10^6$]	$\dot{m}$ [kg/s]	$\dot{W}$ [kW]
10	medium	15	5.41	0.1714	1.4604
	finest	20	8.28	0.1716	1.4477
80	medium	15	5.43	0.4628	3.4579
	finest	20	9.85	0.4627	3.4540
GCI (10% VGT medium core and 15 boundary layer) [%]				0.26	1.96
GCI (80% VGT medium core and 15 boundary layer) [%]				0.02	0.15

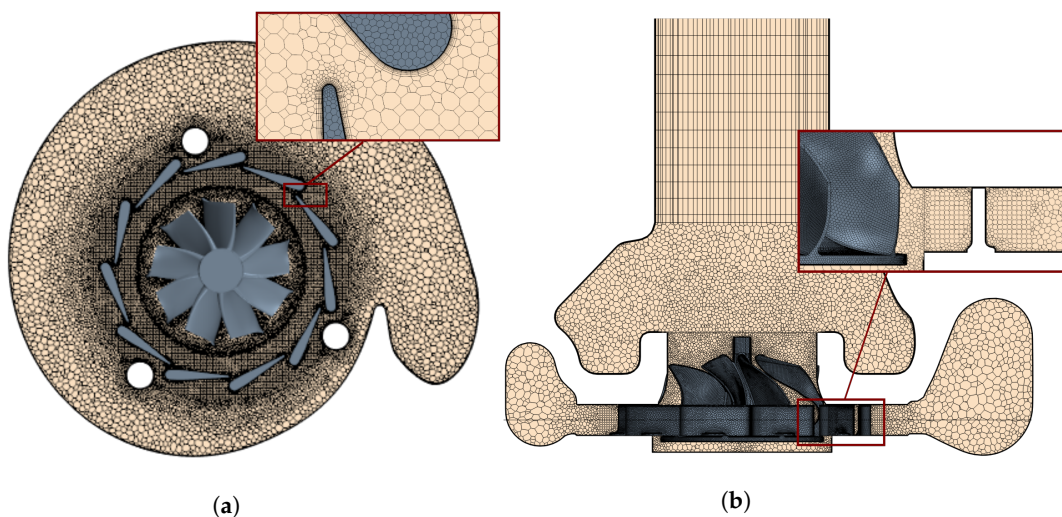(**a**)　　　　　　　　　　　　　　　　　　　　　　　(**b**)

Figure 5. Views of the turbine mesh. (**a**) Top view of the meshed geometry; (**b**) Front view of the meshed geometry.

Table 3. Boundary conditions.

N [rpm]	Ref. PR	$p_{tot.in.}$ [bar]	$p_{stat.out.}$ [bar]	$T_{tot.in.}$ [K]
71,647.86	lower	3	1	340.55
	higher	5.5	1	340.55
155,412.25	lower	3	1	340.55
	higher	5.5	1	340.55

4. Results and Analysis

4.1. Performance Characteristics

The reduced mass flow (Equation (2)) and the total-to-static isentropic efficiency (Equation (3)) at the opened VGT position of all simulated operating points with URANS are depicted in Figure 6. These data correspond to reduced speeds of 3882 (lower speed), 5830 (medium speed), and 8421 rpm/$\sqrt{K}$ (higher speed). The RANS results obtained with the original geometry of +0 pTG evaluated at low and high pressure ratios are included in the figure to remark the trend of the operational points at a constant rotational speed. Furthermore, the figure shows the experimental results obtained in the typical measurement range of automotive turbocharger turbines [52], which operate at low PR compared with the conditions of this study but are presented to obtain a qualitative validation of the simulation results. The rotational speed of 5830 rpm/$\sqrt{K}$ (medium speed) is included in the figure to have more available data and validate them with the trends of the experimental points but is not shown for the analysis of the effects of varying the tip gap. Figure 6a shows that the reduced mass flow increases for the rising tip gap as the pressure losses decrease. At a lower speed, the higher the tip gap is, the higher the PR obtained due to a reduction in the static pressure at the probe section. In addition, at a lower speed, with the rising tip gap, a higher turbine enthalpy drop is needed to drive the rotor at a constant speed. While at a higher speed, the increase in the tip gap generates a decrease in the PR as the static pressure close to the rotor TE increases. At higher speed, the flow behavior through the tip gap is quite different compared with the case at lower speed and will be analyzed in more detail in Section 4.2. Regarding the isentropic efficiency, it decreases when enlarging the tip gap, as shown in Figure 6b against the blade speed ratio (BSR), defined in Equation (4). The reduction in the efficiency is due to the generation of entropy as the flow through the tip gap mixes with the main flow.

$$\dot{m}_{red.,in} = \frac{\dot{m} \cdot \sqrt{T_{t,in}}}{p_{t,in}} \tag{2}$$

$$\eta_{t,s} = \frac{T_{t,in} - T_{t,out}}{T_{t,in} \cdot \left[1 - \left(\frac{1}{\pi_{turb.}}\right)^{\frac{\gamma-1}{\gamma}}\right]} \tag{3}$$

$$BSR = \frac{N_{red} \cdot \pi \cdot D_{in}}{60 \cdot \sqrt{2 \cdot c_{p,turb.} \cdot \left[1 - \left(\frac{1}{\pi_{turb.}}\right)^{\frac{\gamma-1}{\gamma}}\right]}} \tag{4}$$

Table 4 presents the deviation of the PR, the reduced mass flow, and the efficiency with respect to the original geometry of +0 pTG. An improvement of around 1.5% points can be achieved with a reduction in the tip gap of 50% at lower speed, while at higher speed, the increase in the efficiency is almost 3%. Furthermore, a rise of 50% in the gap penalizes the efficiency up to 3% when the turbine operates at lower PR and higher speed.

The enlargement of the area of the plane at the rotor TE as a consequence of the increase in the tip gap contributes to the increase of the reduced mass flow and affects the sonic conditions at this plane. Figure 7 depicts the relation between the reduced mass flow

and the area ratio under supersonic conditions. On the one hand, at lower speed, a lack of an explicit trend is observed, implying that there is no substantial impact on the choked area as the tip gap increases. On the other hand, at higher speed, the growth of the tip gap reduces the choked area. To dive deeper into this phenomenon, the behavior of the flow through the tip gap is first analyzed, where different regions can be distinguished. These regions correspond to the positive and negative tip leakage streams, where the negative flow (scraping flow) is caused by the relative case motion and goes from the SS to the PS [34]. In contrast, the positive flow is driven by the pressure difference between PS and SS. The negative and positive tip leakage mass flows can be evaluated according to Equations (5) and (6), and are summed in Equation (7) [35] to analyze the impact as the tip gap varies. Figure 8 shows how the ratio of the tip leakage on the SS of the gap and the turbine inlet mass flow rises with the enlargement of the tip gap at constant rotational speed. The maximum ratio is 1.05%, which occurs in the case of +50 pTG at lower speed and higher PR. That means that 1.05% of the stage mass flow rate does not contribute to driving the rotor of the radial inflow turbine. Concerning the original geometry of +0 pTG, the relative mass flow that passes the gap decreases around 50% and increases around 60% for the cases with −50 pTG and +50 pTG respectively. Furthermore, as the rotational speed goes from the lower to the higher value, in the operational conditions of lower PR as well as for higher PR, the value of the relative mass flow slightly drops, being 6% for the highest fall for the case of −25 pTG at lower PR and reaching a higher speed, while for the case of +50 pTG at higher PR the ratio remains constant. From the point of view of increasing the PR at a constant speed, growth in the relative mass flow can also be observed; however, some operational conditions generate a different behavior. The following points stand out: −50 pTG at higher speed with growth of 8%, the case of +0 pTG at lower and higher speed without any change, and a decrease of 4%, respectively. This supports the complexity and importance of the tip leakage flow and the impact on the performance parameters at off-design conditions.

Table 4. Variation of the performance parameters with respect to the original geometry (+0 pTG).

$N_{red.}$ $[\frac{rpm}{\sqrt{K}}]$	Ref. PR	Tip Gap	Dev. $\pi_{turb.}$ [%]	Dev. $\dot{m}_{red.}$ [%]	$\Delta\eta_{t,s}$ [% Points]
3882	lower	−50 pTG	−0.79	−0.84	1.55
		−25 pTG	−0.35	−0.25	0.76
		+0 pTG	0	0	0
		+50 pTG	1.08	0.21	−1.27
	higher	−50 pTG	−0.44	−0.79	1.62
		−25 pTG	0.05	−0.67	0.73
		+0 pTG	0	0	0
		+50 pTG	0.92	0.03	−1.08
8421	lower	−50 pTG	1.28	−0.83	2.70
		−25 pTG	0.41	−0.31	1.34
		+0 pTG	0	0	0
		+50 pTG	−1.34	1.25	−3.07
	higher	−50 pTG	2.70	−2.70	2.99
		−25 pTG	1.95	−2.03	1.93
		+0 pTG	0	0	0
		+50 pTG	−0.35	−0.48	−1.27
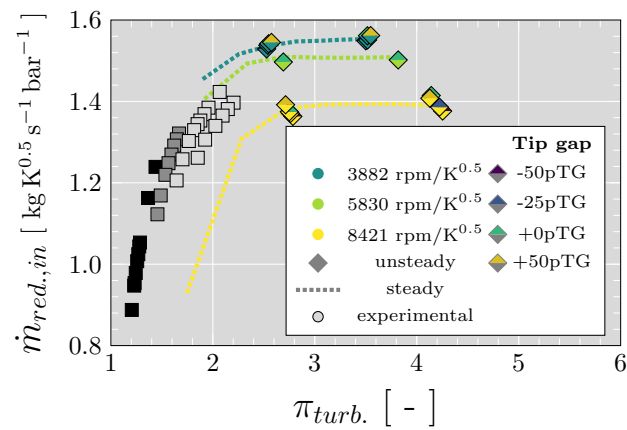
(**a**) Reduced mass flow map.
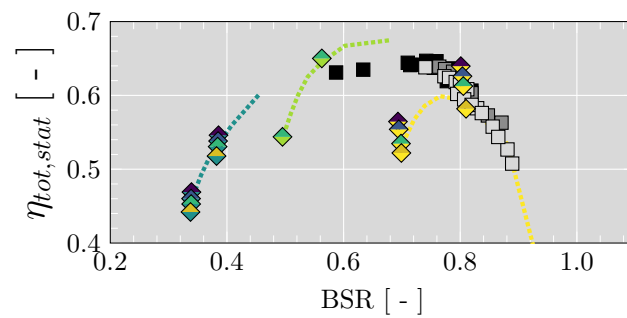
(**b**) Efficiency vs. BSR map.
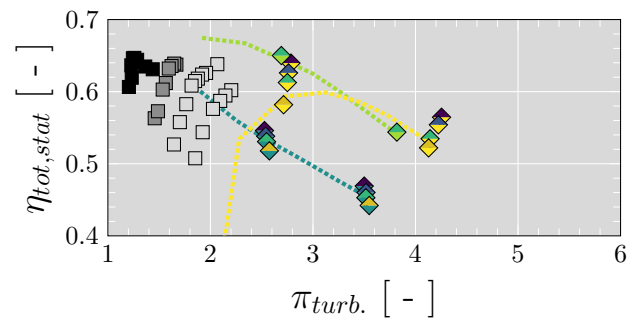
(**c**) Efficiency vs. PR map.

Figure 6. Turbine map based on steady and unsteady results; Steady: Dashed lines; Unsteady: Colored markers; Experimental 3882 rpm/$\sqrt{K}$: black; Experimental 5830 rpm/$\sqrt{K}$: dark gray; Experimental up to 7456 rpm/$\sqrt{K}$: light gray.
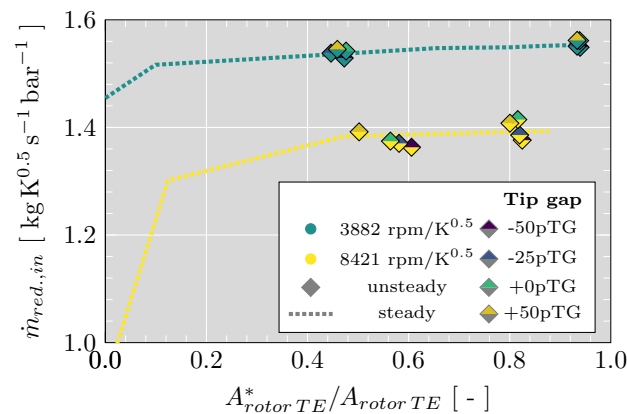

Figure 7. Impact of the area ratio under supersonic conditions on the reduced mass flow.

$$\frac{\dot{m}_{tip,-}}{\dot{m}_{turb.}} = \frac{|\int \rho \cdot \omega_{\perp,tip.-} \cdot dA_-|}{\dot{m}_{turb.}} \tag{5}$$

$$\frac{\dot{m}_{tip,+}}{\dot{m}_{turb.}} = \frac{\int \rho \cdot \omega_{\perp,tip.+} \cdot dA_+}{\dot{m}_{turb.}} \tag{6}$$

$$\frac{\dot{m}_{tip}}{\dot{m}_{turb.}} = \frac{\dot{m}_{tip,-}}{\dot{m}_{turb.}} + \frac{\dot{m}_{tip,+}}{\dot{m}_{turb.}} \tag{7}$$
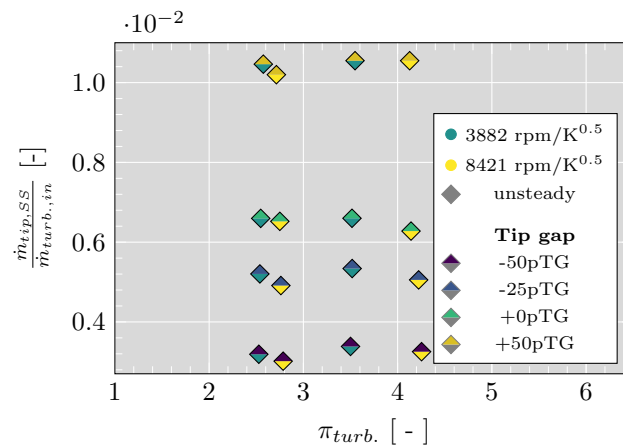

Figure 8. Relative mass flow fraction passing through the tip gap along the SS. The first two vertical lines of points correspond to lower PR and the last two vertical lines of points correspond to higher PR.

4.2. Characteristics of Flow through the Tip Gap

A meridional plane along the tip gap is used to analyze the tip leakage flow. First, the results from the case of +0 pTG at lower PR and both rotational speeds will be analyzed. Considering Figure 9, it can be seen that the flow accelerates when going from the PS to the SS. At lower speed, as shown in Figure 9a,c, the positive flow covers most of the tip gap area. At higher speeds a considerable velocity gradient appears, as shown in Figure 9b,d; these gradients are due the shroud friction that induces the negative flow on the tip gap with the normal component of the relative velocity diminishing as the flow goes from the SS to the PS. The decrease of the positive tip leakage in the rotor inlet region might also be caused by a relative rotor inlet angle with a higher negative incidence [35]. Regarding the development of sonic conditions, at both rotational speeds the flow entering through the PS close to the TE already presents a relative Mach number above one and accelerates further as the flow reaches the SS, especially in the region between 0.75 and 1.0 axial relative length close to the shroud.

Focusing on the region of the tip gap along the SS, a more significant change occurs when the rotational speed increases instead of an increase in the PR, as shown in Figure 10. When the PR rises at both rotational speeds, and thus the blade loads, the expected increase in the positive leakage flow is visible over the tip gap. Nevertheless, the case of a higher rotational speed presents a reduction in the extension of the negative flow along the axial direction. Thus, the ratio between the negative tip leakage mass flow rate and inlet mass flow rate at higher speed decreases around 23% when the turbine operates at higher PR with a corresponding increase in the positive tip leakage. At higher speed, the entire region between 0.75 and 1.0 axial relative length becomes supersonic and the extension changes rather less when the PR rises. When the tip gap varies a similar behavior can be observed.
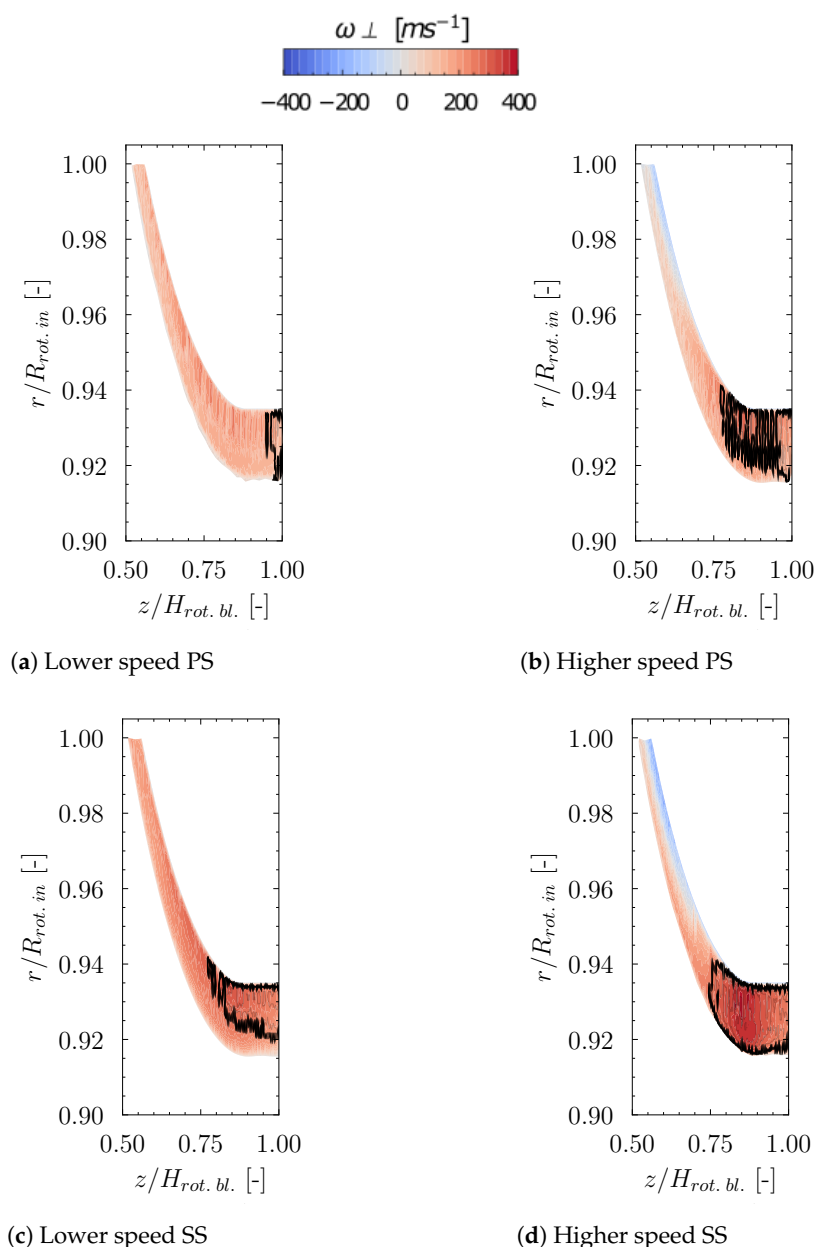
Figure 9. Normal component of the relative velocity on the rotor tip PS and SS for the case of +0 pTG at lower PR; black lines enclose the regions with *Rel. Mach* ≥ 1; URANS simulations; the value equal to 1.0 in the abscissa represents the position of the TE.

To analyze the mass flux in the normal direction through the gap and the effects of the variation the tip gap, Figure 11 is presented for the cases at lower PR and both rotational speeds. Based on the left side of Figure 11, it is possible to observe that at lower speed the negative flow does not change significantly despite the growth in the tip gap, due to the relative motion of the flow close to the shroud wall remaining constant. The location of maximum positive flux remains in the region around 0.95 relative radial length and 0.85 relative axial length, but its magnitude is increased as the tip gap grows. Furthermore, close to the TE ($z/H_{rot.\,bl.} = 1$) the mass flow gets higher with the increasing tip gap. The right side of the Figure 11, which corresponds to the higher speed, shows that the negative mass flux fills more than half of the tip gap in the region between the LE and 0.65 relative length in the axial direction. Thus, less positive tip leakage mass flux passes through the tip gap in this region and diminishes even more as the tip gap decreases. This is particularly clear for the case of -50 pTG (Figure 11b), with almost the entire gap occupied with scraping

flow in the inducer region. Hence, during the manufacturing process it is more important to keep small clearances in the exducer than in the inducer in order to affect the efficiency less. Comparing the left and right sides of Figure 11, it can be seen, on the one hand, that losses generated by positive tip flow can be reduced at higher speed, and, on the other hand, new losses must be taken into account by the entropy generated due to the negative tip flow [27]. At higher PR a similar trend as described above can be observed, as Figure 12 shows for the case of +0 pTG. By comparing the results in Figure 11c,d with the results presented in Figure 12, it is possible to state that increasing the PR leads to higher positive mass flux through the tip gap as described by Deng et al. [54] and Serrano et al. [35]. One can state that the negative mass flow is associated with the rotor speed, while the positive mass flow is rather correlated with the PR.

(**a**) Lower speed and lower PR

(**b**) Higher speed and lower PR

(**c**) Lower speed and higher PR

(**d**) Higher speed and higher PR
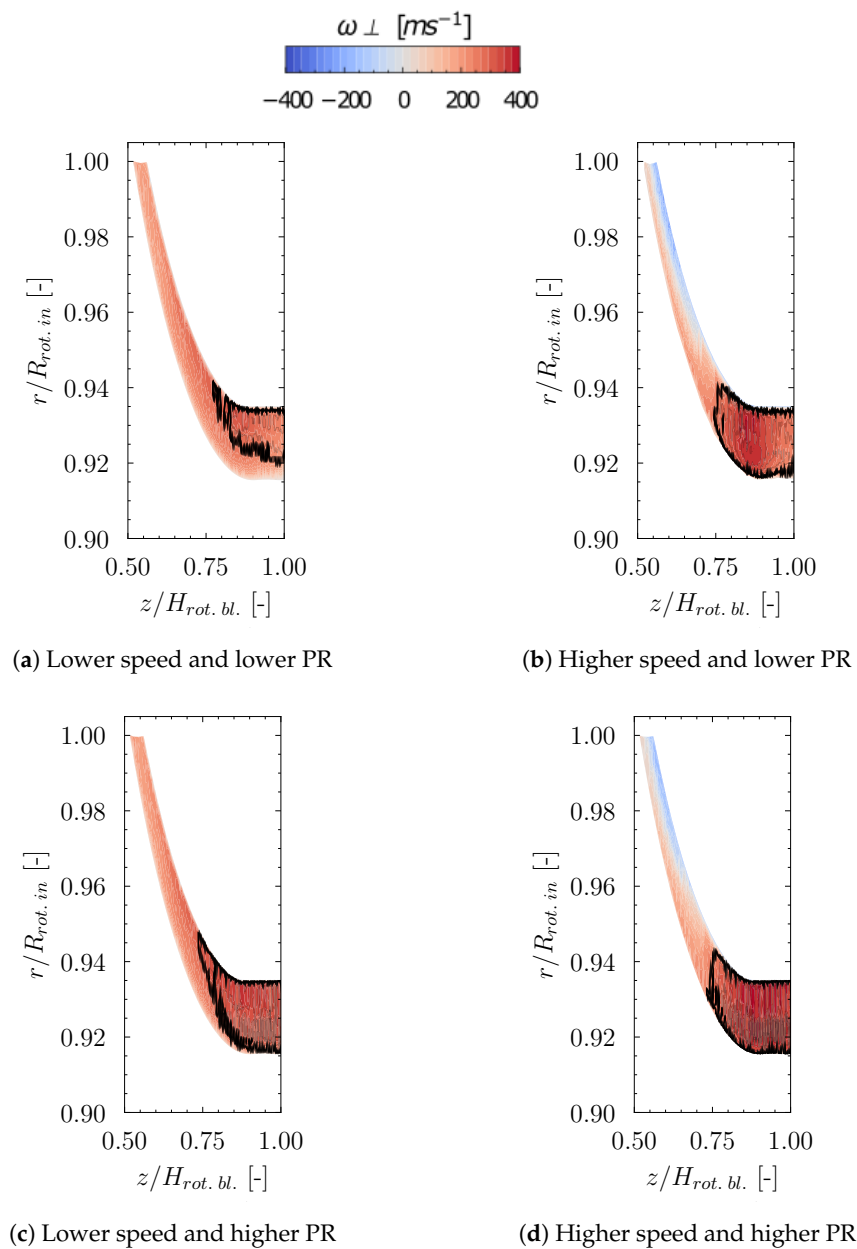
Figure 10. Normal component of the relative velocity on the rotor tip SS for the case +0 pTG. Black lines enclose the regions with *Rel. Mach* $\geq$ 1; URANS simulations. The value equal to 1.0 in the abscissa represents the position of the TE.

(**a**) Lower speed −50 pTG

(**b**) Higher speed −50 pTG

(**c**) Lower speed −25 pTG

(**d**) Higher speed −25 pTG

(**e**) Lower speed +0 pTG

(**f**) Higher speed +0 pTG

(**g**) Lower speed +50 pTG

(**h**) Higher speed +50 pTG
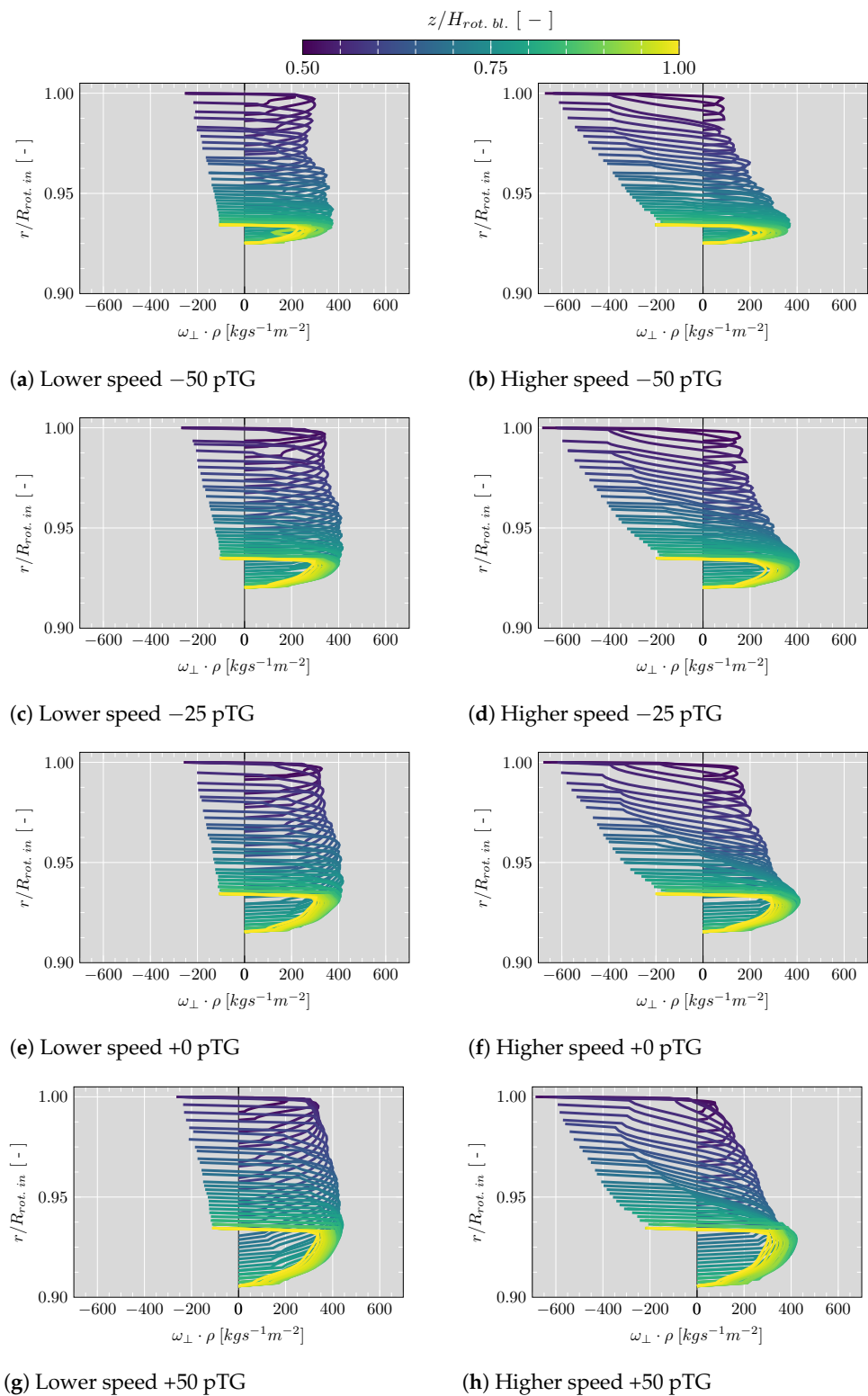
Figure 11. Mass flux on SS at lower PR and both rotational speeds; URANS simulations.

(**a**) Lower speed   (**b**) Higher speed

Figure 12. Mass flux on SS at higher PR for the case of +0 pTG; URANS simulations.

To analyze the sonic conditions along the tip gap at the SS, the meridional red line indicated in Figure 1 was selected to evaluate different parameters. For the aforementioned line and the geomet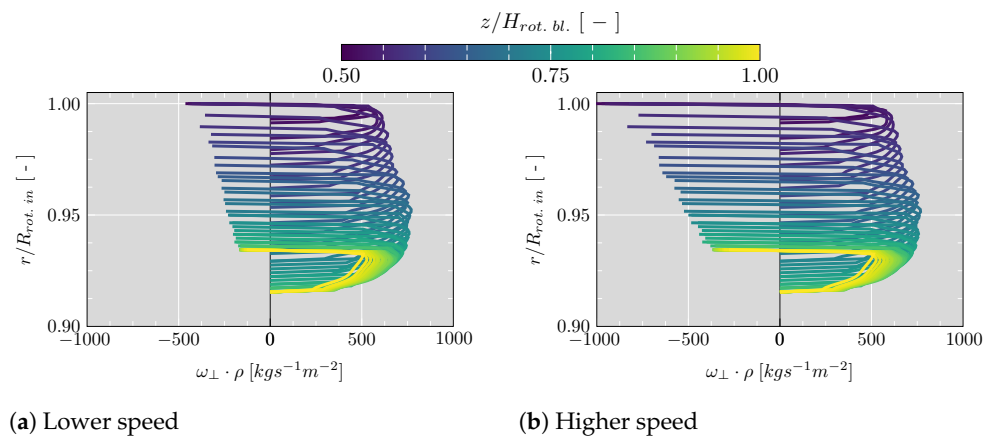ry of +0 pTG, Figure 13a shows the evolution of the relative Mach number. At higher PR and both rotational speeds, the sonic condition is reached at 0.75 relative axial length, while at lower PR it shifts downstream. The peak at 0.87 relative axial length is due to the fact that the relative velocity is normal to the gap, as can be seen in Figure 13b, where at a higher speed it is possible to identify three regions. For the first one, which is near the LE at 0.55 relative axial length, the relative motion of the casing (perpendicular to the blade) is high and thus dragged flow through the gap creates negative tip leakage. The second region appears as the flow moves downstream. Here, the shroud relative motion has been decreased due to the reduced radius, whereas the local blade angle at the tip has increased. Thus, negative tip leakage perpendicular to the blade is decreased, and the positive tip leakage becomes more important as the blade loading over the tip increases, as will be shown further [55]. The third region is a drop-off in the relative velocity normal to the tip gap in the exducer area, where the scraping action relative to the pressure difference between both sides of the rotor blade has already been reduced [56]. However, at higher PR the dip in the relative velocity normal to the tip gap is less and tends to become constant as the rotor outlet is almost choked. The sonic conditions mentioned above can also be noted with the drop in the static pressure, as shown in Figure 13c, as well as the slight increase in the pressure at the exducer region as a consequence of the reduction in the relative velocity normal to the tip gap. Figure 13d depicts how the relative total pressure remains without a significant change as flow goes through the gap without turning into shaft work. However, the relative total pressure decreases close to the exducer region at higher speed and both PR.
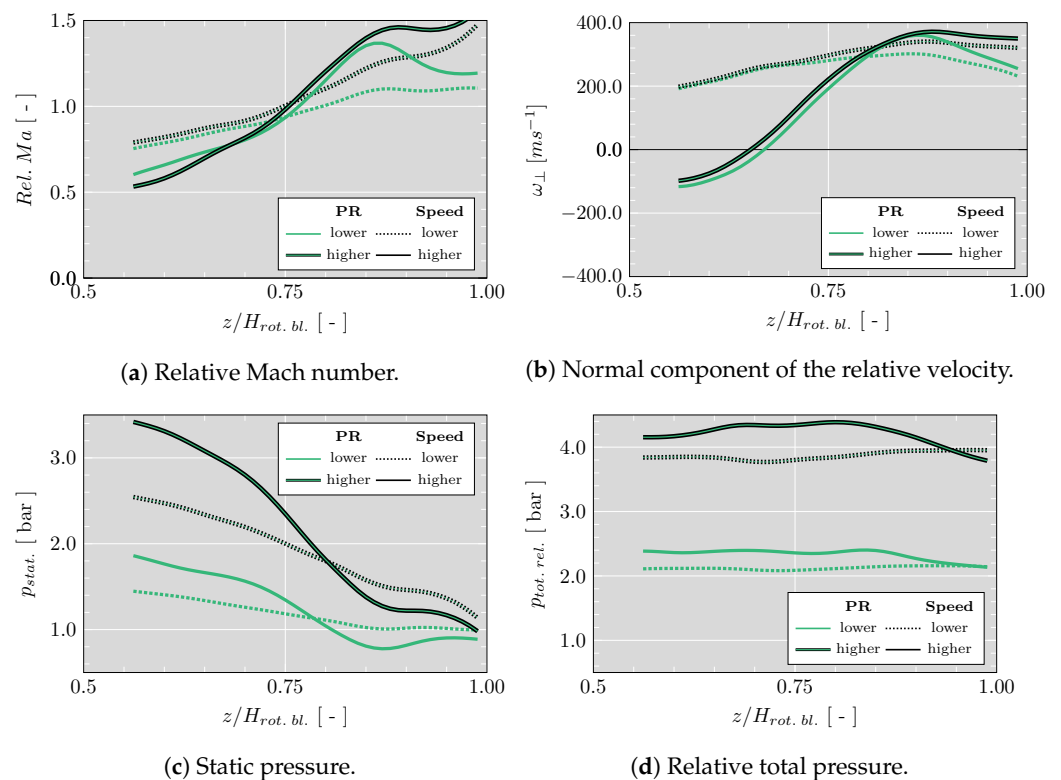
(**a**) Relative Mach number.

(**b**) Normal component of the relative velocity.

(**c**) Static pressure.

(**d**) Relative total pressure.

Figure 13. Flow behaviors for the case of +0 pTG along a meridional line at the middle of the SS tip gap of the −50 pTG case (Figure 1); for the two analyzed PR and two rotational speeds with URANS simulations.

To analyze the impact of the variation in the tip gap on the sonic conditions, the meridional line depicted in Figure 1 is again considered. Figure 14a,b confirms how the flow accelerates when passing from the PS to the SS, especially after 0.75 relative axial length where the blocking effect of the negative tip leakage diminishes and the flow reaches supersonic conditions on the SS. The relative Mach number decreases together with the tip gap, especially for –50 pTG and even more at higher speeds, where the scraping flow is higher than at the rest of the analyzed tip gaps. Considering Figure 14c,d, it is possible to observe that the average difference between the static pressure on the PS and SS (load) along the selected meridional line is slightly greater at lower speed than at higher speed, representing a stronger driving potential for the tip leakage. Furthermore, the difference in the static pressure decreases as the tip gap increases from around 0.75 relative axial length. The lines collapse together as the flow approaches the TE, confirming that the tip leakage flow pattern does not change significantly when varying the tip gap in the exducer region, since the flow here is supersonic. Upstream of the point of 0.75 relative axial length, the driving pressure difference is affected by the negative tip leakage, especially at higher speed. At higher speed, the pressure loading from the inducer drops for all cases except for −50 pTG until a relative length between 0.70 and 0.75; then, the pressure difference starts to increase as the flow continues to accelerate through the tip gap, reaching a higher Mach number. These results reflect the challenge and importance of modeling the effect of negative tip leakage in the inducer and mid-section by means of numerical 1D models, since a successful prediction of the leakage mass flow rate will have a significant impact on turbine losses. The difference in the relative total pressure between PS and SS at lower speed depicted at Figure 14e shows an almost constant trend for all cases except −50 pTG, as the flow through the tip is not used to drive the rotor. However, at higher speed, Figure 14f, the difference presents several fluctuations due to the interactions between the negative and positive tip leakages.
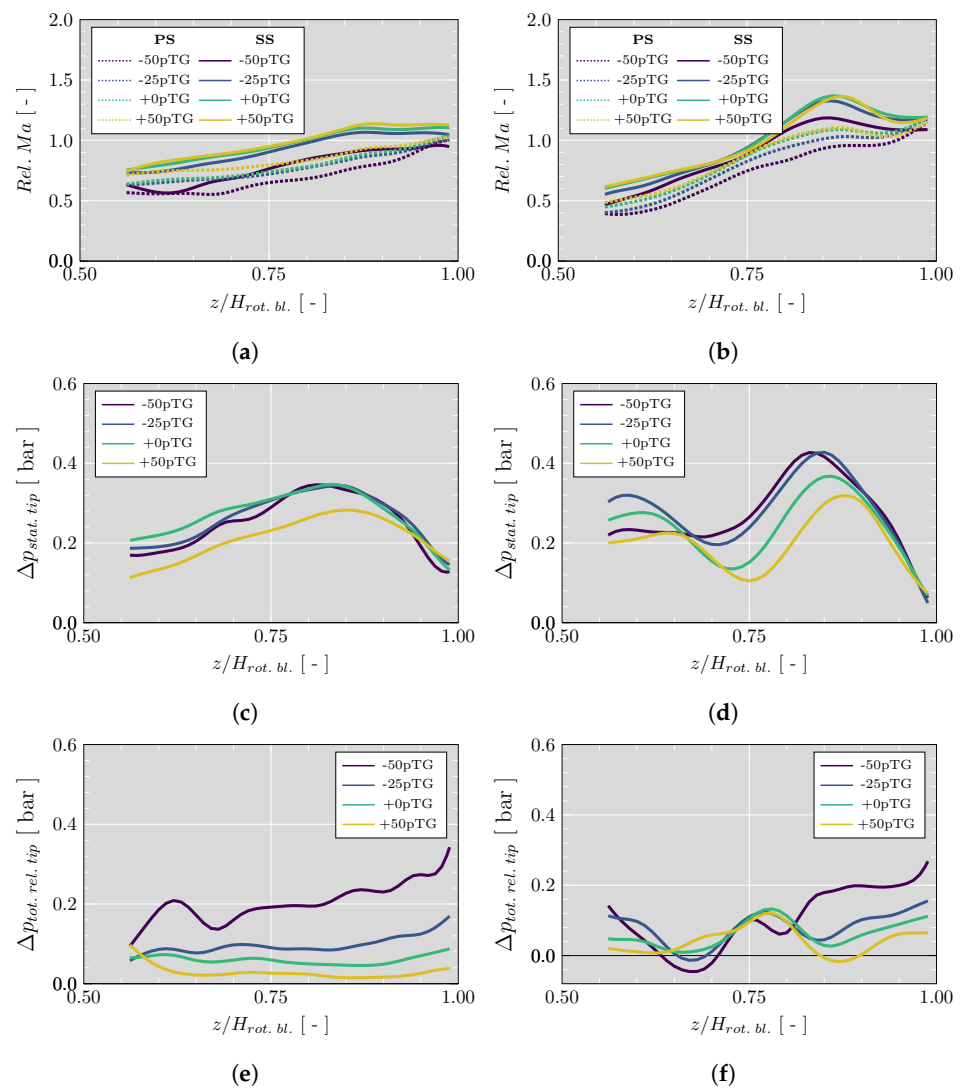
Figure 14. Evaluated variables along a meridional line at the middle of the tip gap of the −50 pTG case (Figure 1) at lower PR; URANS simulations. (**a**) Rel. Ma lower speed. (**b**) Rel. Ma higher speed. (**c**) Static pressure difference between tip PS and SS at lower speed. (**d**) Static pressure difference between tip PS and SS at higher speed. (**e**) Rel. total pressure difference between tip PS and SS at lower speed. (**f**) Rel. total pressure difference between tip PS and SS at higher speed.

4.3. Effects of Tip Leakage on Rotor Blade

PS and SS pressure profiles at 80% and 95% span for different tip gaps both at lower and higher speed for the cases of lower PR are displayed in Figure 15, with the objective of analyzing the impact of the tip leakage on blade loading. The pressure profile of +50 pTG is not considered at 95% span because it does not cover the whole length of the blade. Figure 15a depicts that the pressure difference between the PS and SS of the blade increases from the LE to the TE, with a maximum located between 0.1 and 0.3 relative chord length for the case of lower speed. The pressure at the inducer region increases with rotational speed, Figure 15b. However, the load decreases and the maximum peak occurs around 0.6 relative chord length. Furthermore, the effects on blade loading depends on the span location. As the thickness of the blade decreases from the hub to the shroud, the load increases in the same direction at a higher speed, as shown in Figure 15b,d, while at q lower speed the load decreases from 80% to 95% rotor span as shown in Figure 15a,c. Figure 15 also depicts that a reduction in the tip gap height at lower speed and 80% span does not significantly affect the pressure profile on the PS. although it generates a slight increase of the pressure on the SS from 0.6 to 1.0 relative chord length, while at 95% span

the pressure decrease slightly on the PS from 0.6 to 1.0 relative chord length. At higher speed, a reduction in the tip gap height leads to increased pressure on the PS and on the SS, especially at 95% span. As the surface between two pressure curves is an indicator for the specific aerodynamic work of the blade, the changes mentioned above on the PS and SS generate a reduction in the area formed by the PS and SS pressure line, indicating a lower need for blade loading for the same turbine power. Thus, the turbine efficiency rises, decreasing the tip gap heights, as depicted by Figure 6. This impact is more significant at higher speed, as displayed in Table 4. Moreover, at lower speed, the PS relative velocity increases steadily as the static pressure decreases on the PS from the LE to the TE. Along the SS, the static pressure decreases as the relative velocity increases toward the passage throat until reaching sonic conditions (around 0.6 relative chord length (see Figure 15a) and generates a small supersonic pocket on the SS, as depicted in Figure 16, on the left side. At higher speed, the static pressure has a steeper drop than at a lower speed. The rise in the static pressure on the SS due to the supersonic conditions shifts upstream (around 0.4 relative length; see Figure 15b) compared with the case at lower speed. The supersonic pocket extends until the rotor passage outlet and reaches the PS of the neighboring blade at the TE, as shown in Figure 16, right side. Furthermore, the variation of the tip gap height affects the supersonic conditions. The subsonic region close to the TE on the SS extends upstream and slightly in the direction of the neighboring blade as the tip gap increases due to the expansion of secondary flow vortex, explaining the rise in the static pressure at around 0.70 relative chord length presented in Figure 15b.

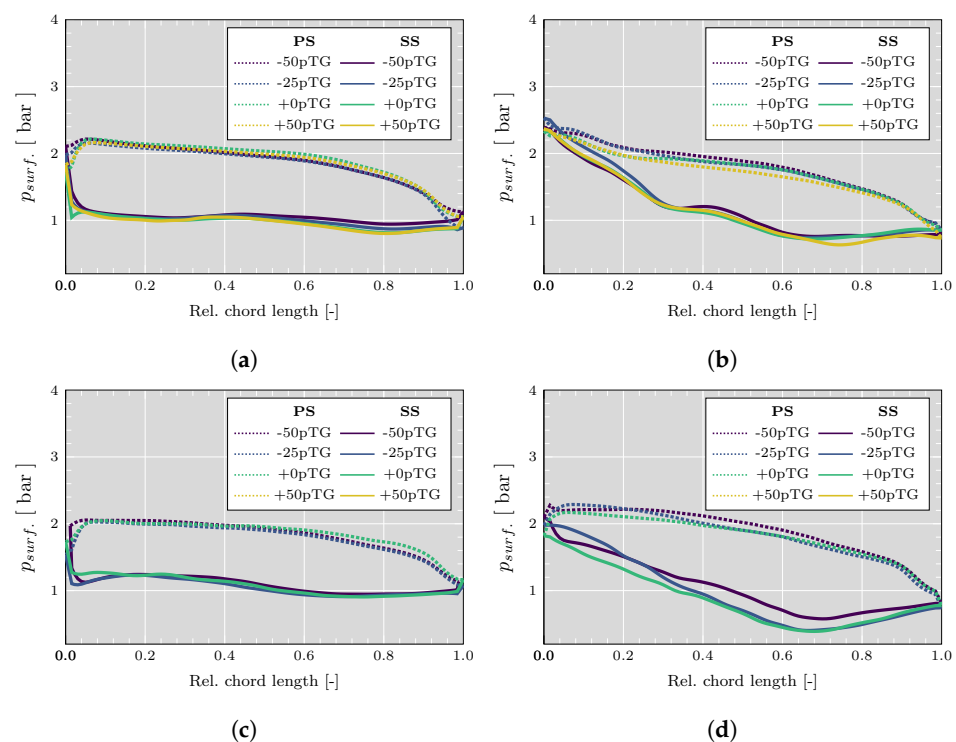**Figure 15.** Rotor static pressure profile at different rotor spans at lower PR; URANS simulations. (**a**) At lower speed and 80% span. (**b**) At higher speed and 80% span. (**c**) At lower speed and 95% span. (**d**) At higher speed and 95% span.
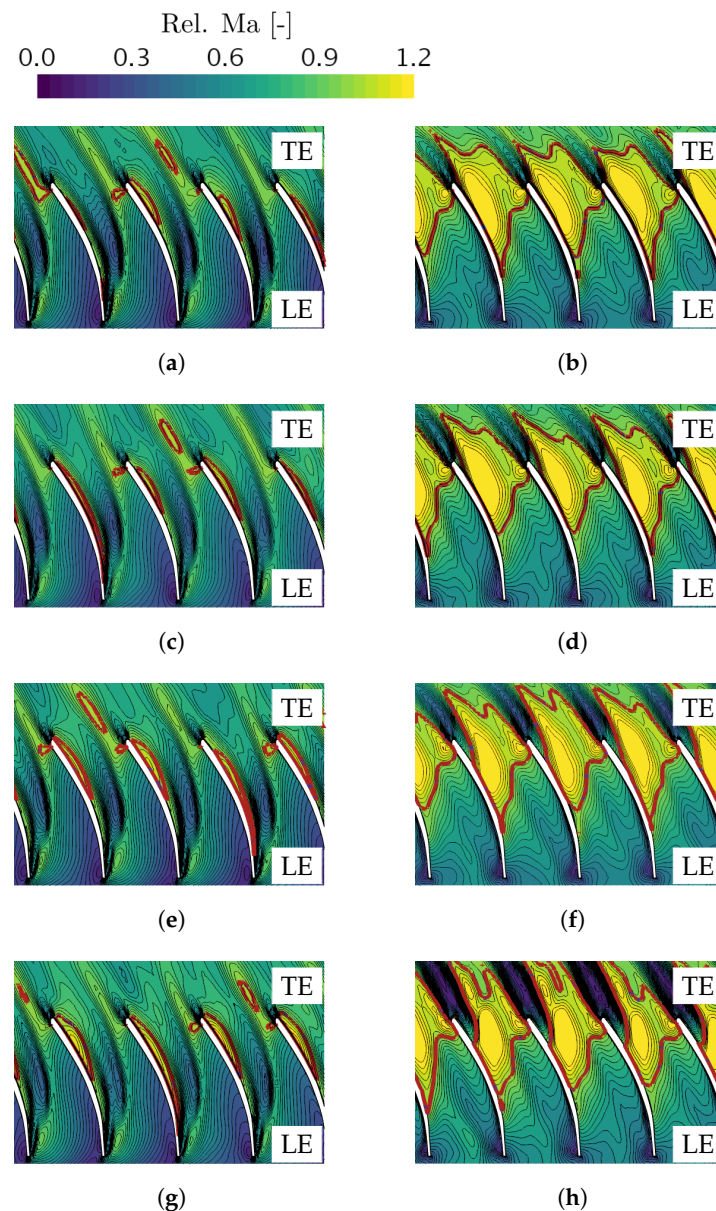
Figure 16. Relative Mach number snapshots at 80% rotor span at lower PR; red line: $Ma_{rel.} = 1$. (**a**) Lower speed -50 pTG. (**b**) Higher speed -50 pTG. (**c**) Lower speed -25 pTG. (**d**) Higher speed -25 pTG. (**e**) Lower speed $+0$ pTG. (**f**) Higher speed $+0$ pTG. (**g**) Lower speed $+50$ pTG. (**h**) Higher speed $+50$ pTG.

At lower speed, the high velocity of leakage flow from the gap in the exducer region blends with the passage main flow and forms a passage vortex [56,57], generating a subsonic region at rotor TE, as depicted in Figure 17 (left side) [36]. However, the increase in the tip gap height does not affect the choked area at the TE significantly, as discussed in Figure 7. At higher speed, in the mid-section and exducer regions, the leakage velocity in the tip gap is less sensitive than that of the inducer region to relative casing motion, which generates negative tip leakage. Furthermore, the vortex created by the interaction between the tip leakage and the mean flow through the channel is pushed towards the blade SS, generating a small subsonic region, so that the formation and development of the leakage vortex are restrained owing to the high relative motion of the shroud, i.e., influenced by the centrifugal force [25,58]. Thus, the rise in the tip gap impacts the choking conditions at the rotor TE as the subsonic region close to tip SS increases, as shown in Figure 17 (right side) and Figure 7. Furthermore, according to Dambach et al. [33], the mixing of the tip leakage

flow with the main stream at the gap exit generates entropy, contributing up to a third of the efficiency loss in a turbine. This loss is proportional to the tip mass flow rate and the velocity components between the mainstream and tip leakage [29,59]. The behavior mentioned above discloses the cause of the lower efficiency at lower speed and how it drops further as the tip gap increases, in accordance with Figure 6b.
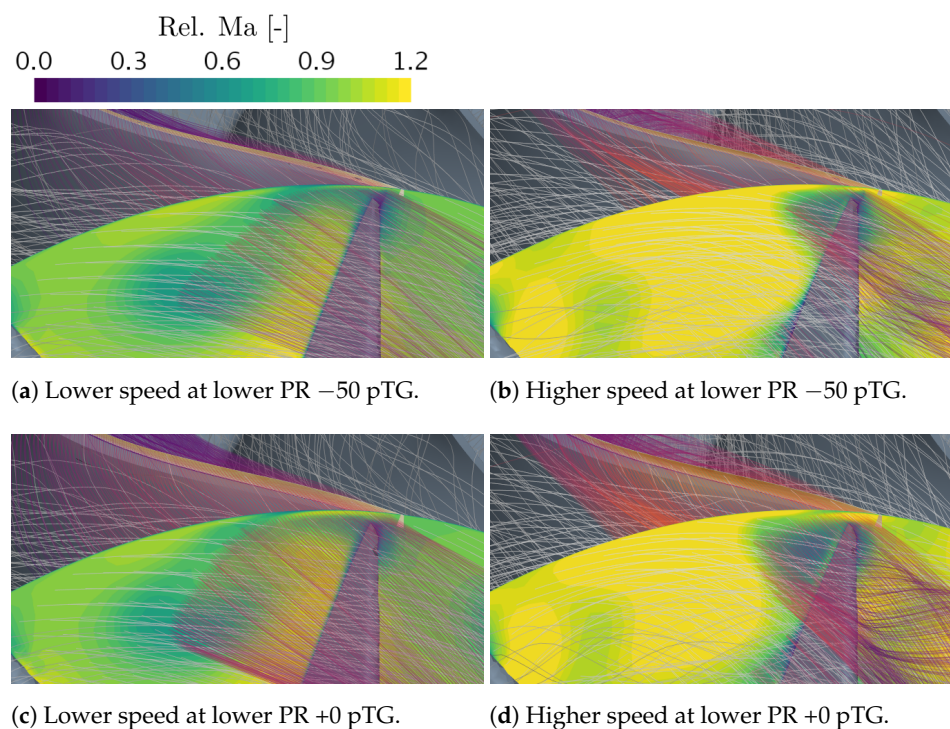

(**a**) Lower speed at lower PR −50 pTG.

(**b**) Higher speed at lower PR −50 pTG.

(**c**) Lower speed at lower PR +0 pTG.

(**d**) Higher speed at lower PR +0 pTG.

Figure 17. Relative velocity streamlines RANS simulations through the rotor tip and rotor TE. Gray streamlines: Main flow from rotor passage. Inferno streamlines: Flow from tip PS.

4.4. Impact of the Varying the Tip Gap on the Main Flow

Two streamlines in the relative reference frame of rotation and with an origin point based on the original geometry of +0 pTG at lower speed are used to analyze the effects of the variation of the tip gap height on the flow through the blade channel, especially in the supersonic region at the TE, as depicted in Figure 18. At lower speed, the first streamline has the origin point at the subsonic region close to the shroud, and the second streamline at the supersonic region close to the hub. The exact coordinates of these points are used for the streamlines at higher speed. The streamlines go through the rotor channel without passing through the tip gap. Furthermore, the streamlines closer to the shroud and the hub show a negative and positive relative angle of attack , respectively, for the cases at lower speed, while at higher speed, the relative angle of attack is negative for both streamlines. This negative incidence reduces the acceleration on the SS, avoiding the choking at the inducer region of the spans, as depicted in Figure 16 [60], and generates a swirl in the streamline close to the shroud downstream of the LE. The reduction in the tip gap does not affect significantly the path followed by the streamlines. However, when the tip gap increases to +50 pTG at lower speed, the streamline at the shroud shifts closer to the PS at the rotor inlet due to the high incidence and separation bubble on the SS, then approaches closer to the SS, where it is deflected to the middle of the channel by the high momentum of the tip leakage, while at higher speed, it presents a reduction in the swirl. Different parameters along the streamlines are considered and depicted in Figure 19 to evaluate more in detail the characteristics of the flow. Significant changes occur at the shroud for the tip gap of +50 pTG, whereas the flow close to the hub remains unchanged despite the variation in the tip gap, following the path of the channel and with a longer axial length. At lower speed, as shown in Figure 19a, the vortex generated at the shroud close to the TE prevents the flow

from reaching a relative Mach number above one. Furthermore, this induced large mixing loss generates a reduction in the static pressure. On the contrary, the flow close to the hub continues accelerating and reaches sonic conditions, with a corresponding drop in the static pressure, as presented in Figure 19c. At higher speed, the strong relative motion of the shroud forces the vortex to stay closer to the tip gap SS rather than in the middle of the channel, as occurs at lower speed. Furthermore, the induced drag by the relative motion of the casing wall causes the flow close to the shroud to accelerate more than the flow close to the hub, so that the flow near the shroud reaches supersonic conditions at the TE, as shown in Figure 19b, with a subsequent drop in the static pressure, as shown in Figure 19d.

(**a**) Lower speed at lower PR −50 pTG. (**b**) Higher speed at lower PR −50 pTG.

(**c**) Lower speed at lower PR −25 pTG. (**d**) Higher speed at lower PR −25 pTG.

(**e**) Lower speed at lower PR +0 pTG. (**f**) Higher speed at lower PR +0 pTG.

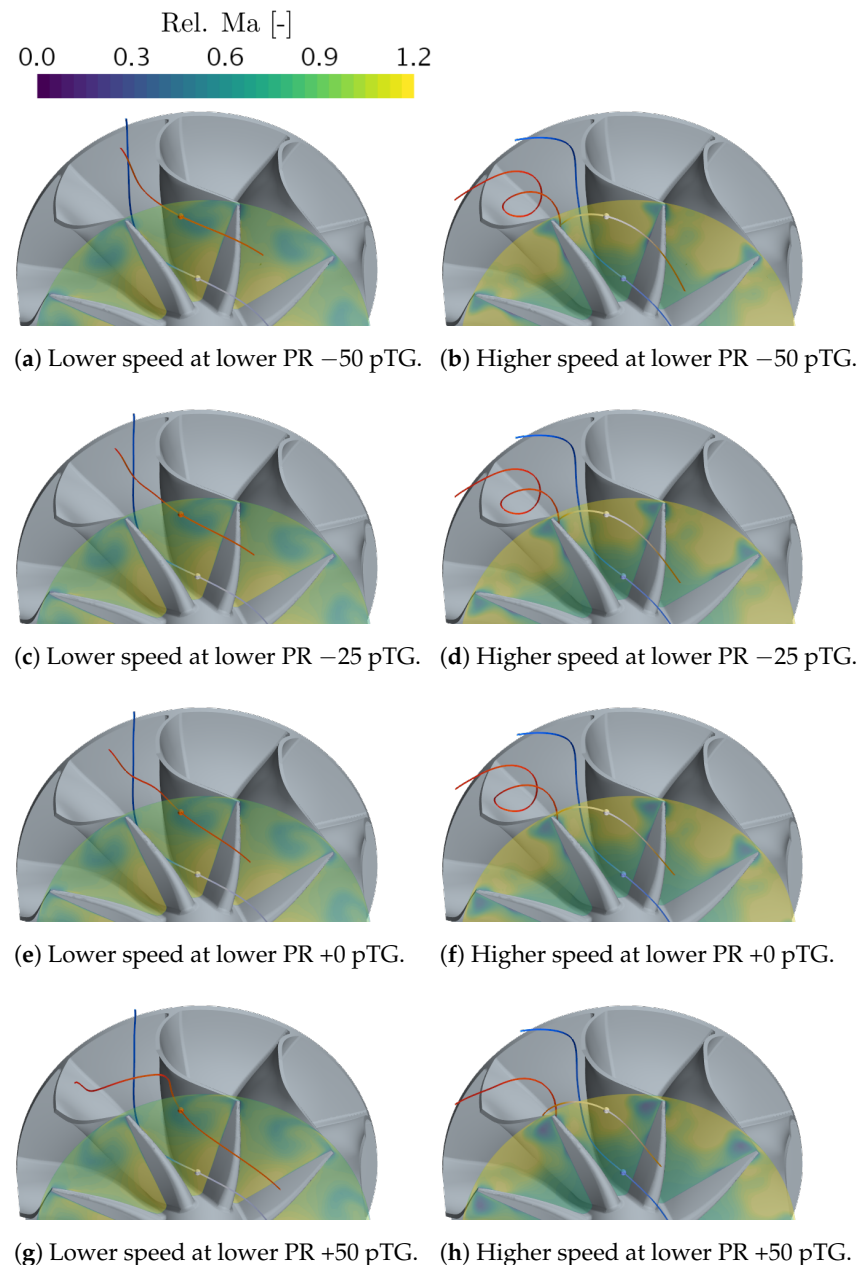(**g**) Lower speed at lower PR +50 pTG. (**h**) Higher speed at lower PR +50 pTG.

Figure 18. Relative velocity streamlines from the rotor TE going through two points. The first one closer to the shroud is the blue streamline and the second one closer to the hub is the orange streamline. RANS simulations.
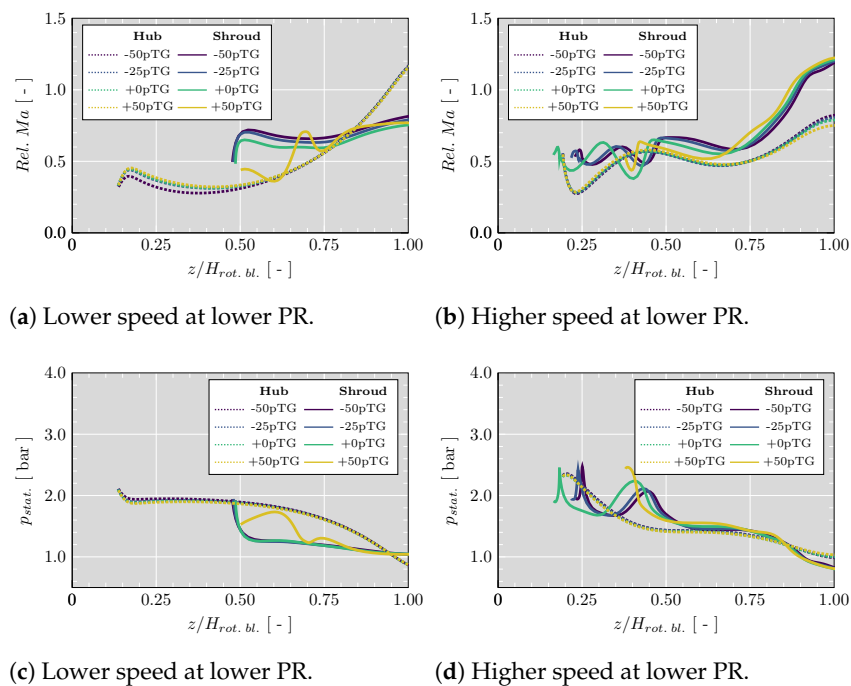
(**a**) Lower speed at lower PR.

(**b**) Higher speed at lower PR.

(**c**) Lower speed at lower PR.

(**d**) Higher speed at lower PR.

Figure 19. Relative Mach number and static pressure evolution along streamlines close to the shroud and hub (Figure 18); the value equal 1.0 in the abscissa represents the position of the TE; RANS simulation.

To dive deeper into the flow behavior and with the intention of analyzing the velocity profile, Figure 20 shows the relative velocity in cylindrical components. The velocity components of the streamline at the hub for both rotational speeds further confirm how the flow remains without any variation despite of the increase in the tip gap height. On the one hand, at lower speed closer to the shroud, the velocity profiles present slight differences except for the case of + 50 pTG. On the other hand, at higher speed and closer to the shroud, the trends are similar but shift downstream as the tip gap decreases. The negative relative incidence angle at the shroud involves a negative tangential velocity (see Figure 20a) and is even greater at higher speed (Figure 20b). At higher speed, the swirl of the flow generates positive and negative fluctuations not only in the tangential velocity but also in the radial velocity. The radial velocity vector at the TE points to the rotor center, represented by the negative value in Figure 20c,d, due to the flow being dragged to the SS by the relative motion of the shroud and then being redirected to the hub as it faces the tip leakage flow. Furthermore, the magnitude of the radial component increases as the tip gap increases. The reduction in the static pressure along the axial direction depicted in Figure 19c,d has a significant impact in the axial velocity at the hub and shroud rather than in the other components of the velocity, as shown by Figure 20e.f. Besides, it is important to remark the higher and uniform flow acceleration at the hub at the lower speed. Regarding the effects produced by the tip gap height, the axial velocity presents higher values at the inducer and middle section as the tip gap decreases, but at the exducer, the axial velocity shows a decline.
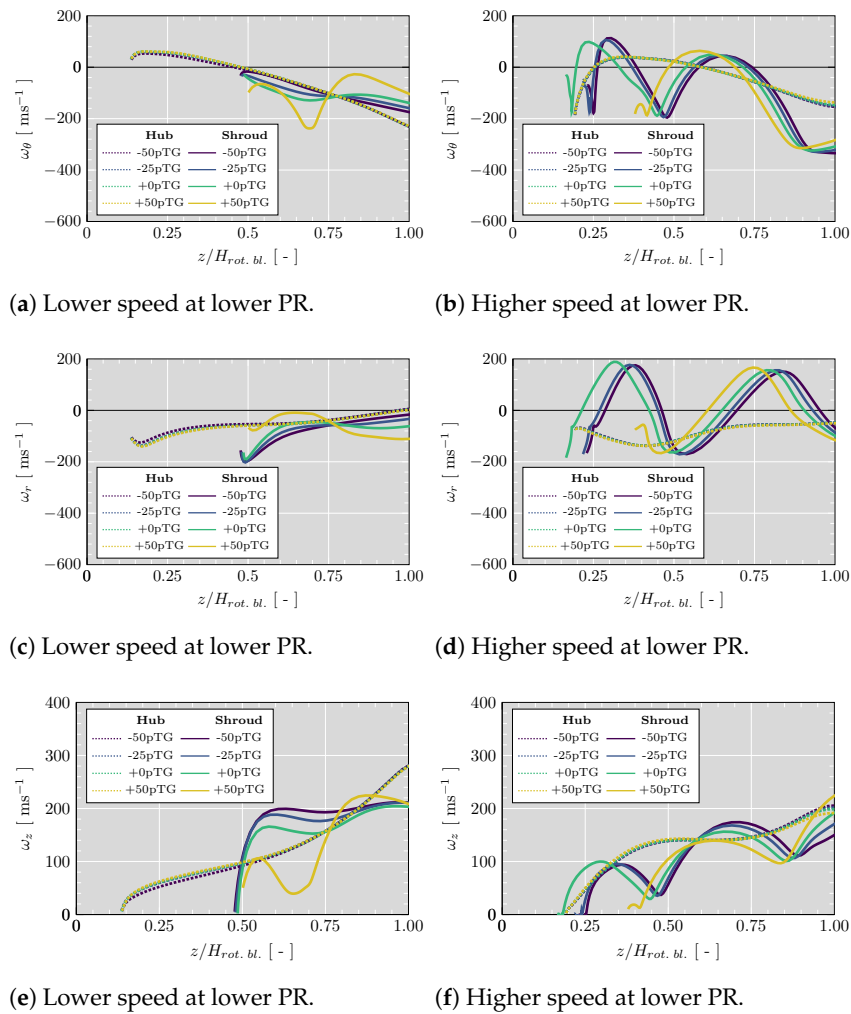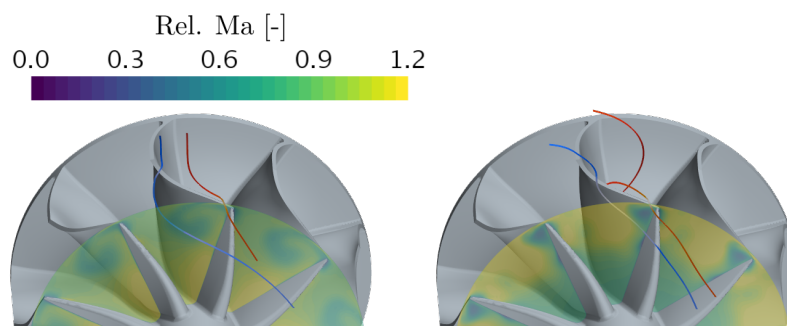
(**a**) Lower speed at lower PR.

(**b**) Higher speed at lower PR.

(**c**) Lower speed at lower PR.

(**d**) Higher speed at lower PR.

(**e**) Lower speed at lower PR.

(**f**) Higher speed at lower PR.

Figure 20. Tangential, radial, and axial component of the relative velocity along the streamlines close to the shroud and hub (Figure 18); the value equal to 1.0 in the abscissa represents the position of the TE; RANS simulation.

4.5. Influence of Tip Gap on Losses

To get a deeper insight into the influence of the changes in the tip gap height over the aerodynamic losses withing the rotor, the entropy generation rate per unit volume provides a good estimation of the location and magnitude of the aerodynamic losses. The entropy generation rate is evaluated using the expression of Ziaja et al. [61], which is based on the definition of Zhang et al. [62] and the work of Moore et al. [63], resulting in Equation 8. The first term of the equation accounts for losses due to molecular and turbulent viscous dissipation and the second term estimates irreversible heat flux.

$$\dot{s}_{gen} = \frac{1}{\bar{T}} \left(\bar{\tau}_{ij} \frac{\partial \bar{u}_i}{\partial x_j} + \frac{\mu_t}{\mu} \frac{\partial \bar{u}_i}{\partial x_j} \right) + \frac{\lambda}{\bar{T}^2} \left(\frac{\partial \bar{T}}{\partial x_i} \cdot \frac{\partial \bar{T}}{\partial x_i} \right) \tag{8}$$

An analysis is performed along two streamlines going through the tip gap at lower and higher speed, both at lower PR. The first streamline goes through the gap closer to the inducer region, while the second streamline passes the gap closer to the exducer, as shown in Figure 21.

(**a**) Lower speed at lower PR +0 pTG.   (**b**) Higher speed at lower PR +0 pTG.

Figure 21. Relative velocity streamlines going through two points: the first one closer to the inducer is the blue streamline and the second one closer to the exducer is the orange streamline; RANS simulations.

Figure 22a,b present the normalized entropy generation rate for the streamlines mentioned above. For the streamline passing through the tip gap closer to the inducer at lower speed, the most significant loss, based on the normalized entropy generation rate, appears when the flow goes through the gap, except for the case of + 50 pTG, where besides of the entropy peak on the tip gap, a greater peak occurs when the flow leaves the gap and mixes with the main flow. At the same rotational speed but for the flow passing the gap closer to the exducer, the highest losses occur just at the tip gap, except for the case of −50 pTG, where the entropy generation rate keeps increasing after the flow passes the gap as a consequence of the reduction in the relative Mach number, as depicted in Figure 22c, as the flow approaches the TE passing a subsonic region close to the SS. Overall, the streamlines follow a path close to the shroud and present the higher losses when passing through the gap and increases as the tip gap height decreases. The entropy generation rate is similar for all the analyzed tip clearances before the streamlines enter the gap.

For the cases at higher speed, the losses reach the higher values when the flow goes through the gap closer to the inducer. The losses drop when the flow leaves the gap following a path close to the SS and accelerates, reaching supersonic conditions as Figure 22d shows between the vertical dashed lines. Furthermore, the streamlines that follow the path that passes the gap closer to the exducer present a considerable loss peak when the flow approaches the gap. Contrary to the case of lower speed in the streamline closer to the inducer, the losses increase as the tip gap height increases. It is also important to remark that the incidence losses are small, as can be observed at the beginning of the entropy lines, being lower at higher speed due to the negative incidence angle [64].

The streamlines of Figure 18 are selected to analyze the losses in the main flow at lower and higher speed by means of the entropy generation rate, normalized using the maximum values of the streamlines depicted in Figure 22. Thus, Figure 23 shows that the losses in the main flow closer to the hub at lower and higher speed represent less than 8% of the loss generated with respect to the entropy generated by the flow going through the tip gap.
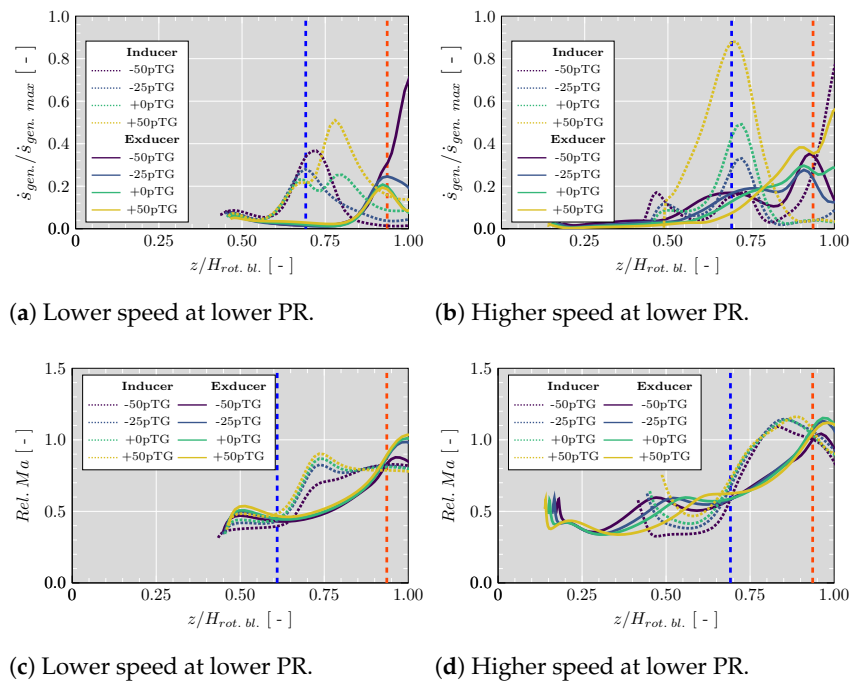
(**a**) Lower speed at lower PR.

(**b**) Higher speed at lower PR.

(**c**) Lower speed at lower PR.

(**d**) Higher speed at lower PR.

Figure 22. Entropy generation rate normalized along streamlines close to the inducer and exducer (Figure 21); the value equals 1.0 in the abscissa and represents the position of the TE. Blue vertical dashed line is the the position where the streamline enters the PS tip gap at the inducer. The orange vertical dashed line is the position where the streamline enters the tip gap PS at the exducer; RANS simulation.
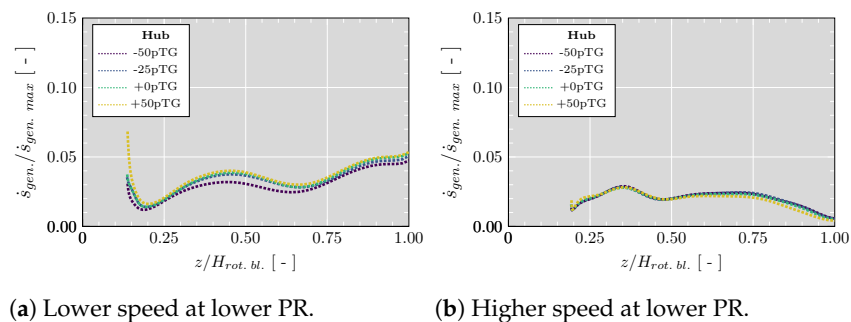

(**a**) Lower speed at lower PR.

(**b**) Higher speed at lower PR.

Figure 23. Entropy generation rate normalized along streamlines close to the hub (Figure 18); the value equals 1.0 in the abscissa and represents the position of the TE; RANS simulation.

5. Conclusions

In this study, a variable geometry turbine of a turbocharger used in commercial automotive engines, with the stator vanes at an opened position operating at two rotational speeds and two PR reaching choking conditions,was selected to characterize the flow through the tip gap and the effects on the main flow through the rotor channel by reducing and increasing the tip gap. The analysis was carried out based on RANS and URANS simulations.

Regarding the performance parameters, the isentropic efficiency decreases when enlarging the tip gap due to the generating entropy as the flow through the tip gap mixes with the main flow, and such a decrease can represent a penalty of even 3% points. Thus, during the manufacturing process, one should try to obtain the smallest possible tip gap, because with a reduction of 50% and even operating at higher speed and higher PR the increase in the efficiency is almost 3% points, which improves the engine performance.

The increase in the tip gap height generates a secondary flow vortex at a higher speed, which stays close to the tip SS, thereby reducing the choked area at rotor TE and increasing

the reduced mass flow. Furthermore, the ratio of the tip leakage mass flow rate and the mass flow at the turbine inlet is lower at higher speed than at lower speed due to the scrapping flow allowing for a higher efficiency.

Regarding the flow dynamics through the gap, the flow accelerates from the PS to the SS, reaching supersonic conditions in the exducer region for all the selected operational points. Furthermore, it is important to highlight that even at lower speed and lower PR the flow entering the PS close to the TE reaches a Mach number greater than one. Furthermore, due to the relative motion of the shroud, the inducer SS drags some of the flow from the casing, causing one part of the flow to be deflected to the hub, and the remaining flow (negative tip leakage or scrapping flow) travels through the tip gap from the SS to the PS. Based on the mass flux through the gap, at lower speed the negative flow does not change significantly despite the growth in the tip gap, and its magnitude is due to the relative motion of the shroud wall. However, at higher speeds, the negative tip leakage is pretty significant in the flow profile of the tip gap, filling almost more than the half of the inducer region and reducing the mass flux of positive tip leakage, which is reduced even more as the tip gap decreases. One can highlight that the negative tip leakage is reduced by increasing the PR and generating an increase in the positive tip leakage but without significantly affecting the extension of the supersonic pocket in the axial direction of the tip. The reduction in the negative tip leakage by the PR increase can even be 23%.

The average difference between the static pressure on the PS and SS along the tip gap is slightly more significant at a lower speed than at a higher speed, representing a higher driven potential for the tip leakage, and must be considered when proposing a correlation to evaluate the losses. Furthermore, the difference in the static pressure decreases as the tip gap increases from around 0.75 relative axial length. However, close to the TE, the difference becomes smaller, confirming that the tip leakage flow pattern did not change significantly when varying the tip gap in the exducer region. Thus, during the manufacturing process it is more important to guarantee a small tolerance in the inducer region. The effects on blade loading depends on the span location, as the thickness of the blade decreases from the hub to the shroud, the load increases in the same direction at higher speed, and at lower speed the load decreases from 80% to 95% rotor span. A reduction in the tip gap height at lower speed does not significantly affect the pressure profile on the PS at 80% span, but generates a slight increase of the pressure on the SS from 60% of the chord length. Thus, the pressure difference rises as the tip gap increases. For all the evaluated tip gaps geometries as the static pressure on the SS decreases, the relative velocity increase generates a small supersonic pocket. At higher speed, a reduction in the tip gap height leads to increased pressure on the PS and on the SS. As in the case of lower speed, a supersonic region appears on the SS but with higher intensity and extends until the rotor passage outlet and reaches the PS of the neighboring blade at the TE. However, the flow remains subsonic close to the TE on the SS due to the secondary vortex that increases with the increasing tip gap height.

By analyzing the interaction between the main flow and the tip leakage for both rotational speeds it is observed that, at lower speed, the vortex created by the blend of the high velocity of the leakage flow and the main flow at the exducer region produces a subsonic region at the TE close to the shroud. However, with the increase in the tip gap height, and thus the relative mass flow, the choked area at the TE is not significantly affected. For the cases at higher speed, a subsonic region appears on the SS at the TE and grows with the tip gap due to the increase of the secondary flow vortex generated by the interaction between the tip leakage and the main flow. Thus, the choked area at TE close to the shroud decreases with the increase of the tip gap height. It is important to remark that the location of the supersonic region close to the shroud is due to the high relative inlet flow angle, swirling flow, and the effects of the high relative motion of the wall at the shroud.

To evaluate the characteristic of the flow in more detail, two streamlines through the blade channel passing close to the shroud and hub were selected. The results showed that a significant change occurs with the increase of the tip gap with respect to the original geometry rather than with the reduction of the gap for the the streamline close to the shroud,

whereas the conditions of the streamline close to the hub, such as the velocity profile, remained almost unaltered and reached choking conditions for the case of lower speed.

An analysis of the aerodynamic losses based on the entropy generation rate through different streamlines showed that at lower and higher speeds, the most significant losses occur when the flow goes through the tip gap close to the inducer and exducer. Furthermore, close to the inducer at lower speed, the losses increase with the reduction in the tip gap height. On the contrary, at higher speed, the losses increase with the tip gap height. The losses in the main flow closer to the hub at lower and higher speeds represent less than 8% of the loss generated with respect to the entropy generated by the flow going through the tip gap.

These results could be employed in the framework of small radial turbines to both improve tip leakage loss models and also to design tip clearance profiles that reduce such losses. The one-dimensional loss model should consider a correlation that evaluates aspects such as the choked area at the tip gap and the effects of the tip leakages vortex on the sonic conditions at the rotor TE and the generated entropy of the flow going through the tip gap and closer to the hub . However, researchers should be aware of the limitations of this study. First, the findings are obtained from a single turbine geometry with different tip gaps but the same tip clearance profile. Therefore, the quantitative results could be case-dependent, but the discussed qualitative trends are expected to be consistent for all small-size radial turbines, due to the similarities in their designs. Besides, despite the efforts to minimize the numerical errors (e.g., by achieving grid independence), the uncertainty of modeling turbulence and neglecting the effects of thermal and rotational deformation in the turbine impeller and shroud still exist.

Author Contributions: Conceptualization, L.B.I.; methodology, L.B.I. and J.D.E.; software, J.D.E; formal analysis, J.D.E; investigation, J.D.E; resources, R.N.; data curation, J.D.E.; writing—original draft preparation, J.D.E.; writing—review and editing, J.G., A.T., R.N., L.B.I. and J.D.E.; supervision, A.T. and L.B.I. All authors have read and agreed to the published version of the manuscript.

Data Availability Statement: The data presented in this study are available on request from the corresponding author.

Conflicts of Interest: The authors declare no conflict of interest. The funders had no role in the design of the study; in the collection, analyses, or interpretation of data; in the writing of the manuscript, or in the decision to publish the results.

Abbreviations

The following abbreviations are used in this manuscript:

Notations

D	Rotor diameter
H	Height
Ma	Mach Number
$\dot{m}$	Mass Flow
$\dot{m}_{red.}$	Reduced Mass Flow
N	Rotational speed
p	Pressure or order of accuracy
r	radial coordinate or refinement factor ratio
R	Radius
$\dot{s}_{gen}$	Entropy generation rate per unit volume
T	Temperature

t	Time
y^+	Non-dimensional wall distance
z	z-coordinate (axial direction)
u	flow velocity

Abbreviations

BSR	Blade speed ratio
CFD	Computational Fluid Dynamics
GCI	Global Convergence Index
LE	Leading Edge
PR	Pressure Ratio
PS	Pressure Side
RANS	Reynolds Average Navier Stokes
SS	Suction Side
TE	Trailing Edge
URANS	Unsteady Reynolds Average Navier Stokes
VGT	Variable Geometry Turbine

Greek symbols

α	Stator Blade Angle
Δ	Difference
ϵ	Relative error
η	Efficiency
λ	Thermal conductivity
θ	Tangential component
π	Corresponding Pressure Ratio
ω	Relative velocity
ρ	Density
μ	Dynamic viscosity
$\bar{\tau}_{ij}$	Viscous stress tensor

Subscripts

$bl.$	Blade
in	Turbine Inlet Section
$red.$	Reduced Numbers
$rel.$	Relative Value
$rot.$	Rotor
s	Static Conditions
$surf.$	Rotor Blade Surface
t	turbulent
tip	Rotor blade tip
tot	Total or Stagnation Conditions
t,s	Total-To-Static Value

Numbers and Symbols

$+$	Positive direction
$-$	Negative direction
$\bar{}$	Averaged
$*$	Choked
$\perp$	Perpendicular

References

1. Mirza-Hekmati, D.; Heath, W.P.; Apsley, J.M.; Forbes, J.R. Down-speeding diesel engines with two-stage turbochargers: Analysis and control considerations. *Int. J. Engine Res.* **2020**, *23*, 78–89. https://doi.org/10.1177/1468087420976482.
2. Jiménez-Espadafor Aguilar, F.J.; Vélez Godiño, J.A. Innovative power train configurations for aircraft auxiliary power units focused on reducing carbon footprint. *Aerosp. Sci. Technol.* **2020**, *106*, 106109. https://doi.org/10.1016/j.ast.2020.106109.
3. Ochoa, G.V.; Isaza-Roldan, C.; Forero, J.D. A phenomenological base semi-physical thermodynamic model for the cylinder and exhaust manifold of a natural gas 2-megawatt four-stroke internal combustion engine. *Heliyon* **2019**, *5*, e02700. https://doi.org/10.1016/j.heliyon.2019.e02700.
4. Ribau, J.; Silva, C.; Brito, F.P.; Martins, J. Analysis of four-stroke, Wankel, and microturbine based range extenders for electric vehicles. *Energy Convers. Manag.* **2012**, *58*, 120–133. https://doi.org/10.1016/j.enconman.2012.01.011.

5. García, A.; Monsalve-Serrano, J.; Martínez-Boggio, S.; Wittek, K. Potential of hybrid powertrains in a variable compression ratio downsized turbocharged VVA Spark Ignition engine. *Energy* **2020**, *195*, 117039. https://doi.org/10.1016/j.energy. 2020.117039.

6. Estrada, L.; Moreno, E.; Gonzalez-Quiroga, A.; Bula, A.; Duarte-Forero, J. Experimental assessment of performance and emissions for hydrogen-diesel dual fuel operation in a low displacement compression ignition engine. *Heliyon* **2022**, *8*, e09285. https://doi.org/10.1016/j.heliyon.2022.e09285.

7. Chiesa, S.; Fioriti, M.; Fusaro, R. Possible hybrid propulsion configuration for transport jet aircraft. *Aviation* **2016**, *20*, 145–154. https://doi.org/10.3846/16487788.2016.1200849.

8. Wittmann, T.; Lück, S.; Bode, C.; Friedrichs, J. Modelling the Condensation Phenomena within the Radial Turbine of a Fuel Cell Turbocharger. *Int. J. Turbomach. Propuls. Power* **2021**, *6*, 23. https://doi.org/10.3390/ijtpp6030023.

9. Altarazi, Y.S.M.; Abu Talib, A.R.; Yu, J.; Gires, E.; Abdul Ghafir, M.F.; Lucas, J.; Yusaf, T. Effects of biofuel on engines performance and emission characteristics: A review. *Energy* **2022**, *238*, 121910. https://doi.org/10.1016/j.energy.2021.121910.

10. Jeyaseelan, T.; Chacko, N.; Pushyanth, N.; Alexander, J.; Porpatham, E. Partial hydrogenation and hydrogen induction: A comparative study with B20 operation in a turbocharged CRDI diesel engine. *Int. J. Hydrogen Energy* **2021**, *46*, 22659–22669. https://doi.org/10.1016/j.ijhydene.2021.04.068.

11. Alshammari, F. Radial Turbine Expander Design, Modelling and Testing for Automotive Organic Rankine Cycle Waste Heat Recovery. Ph.D. Thesis, Brunel University London, Uxbridge, UK, 2018.

12. Permana, D.I.; Rusirawan, D.; Farkas, I. A bibliometric analysis of the application of solar energy to the organic Rankine cycle. *Heliyon* **2022**, *8*, e09220. https://doi.org/10.1016/j.heliyon.2022.e09220.

13. Polanco Piñerez, G.; Valencia Ochoa, G.; Duarte-Forero, J. Energy, exergy, and environmental assessment of a small-scale solar organic Rankine cycle using different organic fluids. *Heliyon* **2021**, *7*, e07947. https://doi.org/10.1016/j.heliyon.2021. e07947.

14. The Effect of Clearance Flow of Variable Area Nozzles on Radial Turbine Performance. In *Turbo Expo: Power for Land, Sea, and Air*; ASME: Berlin, Germany, 2008; Volume 6. https://doi.org/10.1115/GT2008-50461.

15. Izaguirre, A.O.T.; García, R.N.; Inhestern, L.B.; Gómez, N.H. Design and numerical analysis of flow characteristics in a scaled volute and vaned nozzle of radial turbocharger turbines. *Energies* **2020**, *13*, 19. https://doi.org/10.3390/en13112930.

16. Dufour, G.; Carbonneau, X.; Cazalbou, J.b.; Chassaing, P. Practical Use of Similarity and Scaling Laws for Centrifugal Compressor Design. In *Turbo Expo: Power for Land, Sea, and Air*; ASME: Barcelona, Spain, 2006; Volume 6, pp. 1131–1140. https://doi.org/10.1115/GT2006-91227.

17. Galindo, J.; Tiseira Izaguirre, A.O.; García-Cuevas, L.M.; Hervás Gómez, N. Experimental approach for the analysis of the flow behaviour in the stator of a real centripetal turbine. *Int. J. Engine Res.* **2020**, *22*, 1–11. https://doi.org/10.1177/1468087420916281.

18. Binder, N.; Le Guyader, S.; Carbonneau, X. Analysis of the Variable Geometry Effect in Radial Turbines. *J. Turbomach.* **2011**, *134*, 041017. https://doi.org/10.1115/1.4003713.

19. Marsan, A.; Moreau, S. Analysis of the flow structure in a radial turbine. In Proceedings of the 11th European Conference on Turbomachinery Fluid Dynamics and Thermodynamics, ETC 2015, Madrid, Spain, 23–27 March 2015; pp. 1–13.

20. Kan, K.; Binama, M.; Chen, H.; Zheng, Y.; Zhou, D.; Su, W.; Muhirwa, A. Pump as turbine cavitation performance for both conventional and reverse operating modes: A review. *Renew. Sustain. Energy Rev.* **2022**, *168*, 112786. https://doi.org/10.1016/j.rser.2022.112786.

21. Kan, K.; Zhang, Q.; Xu, Z.; Zheng, Y.; Gao, Q.; Shen, L. Energy loss mechanism due to tip leakage flow of axial flow pump as turbine under various operating conditions. *Energy* **2022**, *255*, 124532. https://doi.org/10.1016/j.energy.2022.124532.

22. Kan, K.; Li, H.; Chen, H.; Xu, H.; Gong, Y.; Li, T.; Shen, L. Effects of Clearance and Operating Conditions on Tip Leakage Vortex-Induced Energy Loss in an Axial-Flow Pump Using Entropy Production Method. *J. Fluids Eng.* **2022**, *145*, 031201. https://doi.org/10.1115/1.4056119.

23. Kollek, W.; Osiński, P.; Stosiak, M.; Wilczyński, A.; Cichoń, P. Problems relating to high-pressure gear micropumps. *Arch. Civ. Mech. Eng.* **2014**, *14*, 88–95. https://doi.org/10.1016/j.acme.2013.03.005.

24. Zhao, B.; Yang, C.; Hu, L.; Sun, H.; Yi, J.; Eric, C.; Shi, X.; Engeda, A. Understanding of the Interaction between Clearance Leakage Flow and Main Passage Flow in a VGT Turbine. *Adv. Mech. Eng.* **2015**, *7*, 652769. https://doi.org/10.1155/2014/652769.

25. He, P.; Sun, Z.; Zhang, H.; Chen, H.; Tan, C. Investigation of clearance flows in deeply scalloped radial turbines. *Proc. Inst. Mech. Eng. Part A J. Power Energy* **2012**, *226*, 951–962. https://doi.org/10.1177/0957650912460361.

26. Kammeyer, J.; Natkaniec, C.; Seume, J.R. Tip leakage in small radial turbines: Optimum tip-gap and efficiency loss correlations. In *Turbo Expo: Power for Land, Sea, and Air*; ASME: Glasgow, UK, 2010; pp. 1–11. https://doi.org/10.1115/GT2010-22680.

27. Serrano, J.R.; Navarro, R.; García-Cuevas, L.M.; Inhestern, L.B. Contribution to tip leakage loss modeling in radial turbines based on 3D flow analysis and 1D characterization. *Int. J. Heat Fluid Flow* **2019**, *78*, 1–7. https://doi.org/10.1016/j.ijheatfluidflow.2019.108423.

28. Zhang, Q.; He, L. Over-tip choking and its implications on turbine blade-tip aerodynamic performance. *J. Propuls. Power* **2011**, *27*, 1008–1014. https://doi.org/10.2514/1.B34112.

29. Wheeler, A.P.S.; Korakianitis, T.; Banneheke, S. Tip-Leakage Losses in Subsonic and Transonic Blade Rows. *J. Turbomach.* **2012**, *135*, 011029. https://doi.org/10.1115/1.4006424.

30. Pashayev, A.; Askerov, D.; Sadiqov, R. Numerical modeling of gas turbine cooled blades. *Aviation* **2005**, *9*, 9–18. https://doi.org/10.3846/16487788.2005.9635905.

31. O'Dowd, D.O.; Zhang, Q.; He, L.; Oldfield, M.L.G.; Ligrani, P.M.; Cheong, B.C.Y.; Tibbott, I. Aero-Thermal Performance of a Winglet at Engine Representative Mach and Reynolds Numbers. In *ASME Turbo Expo 2010: Power for Land, Sea, and Air*; ASME: Glasgow, UK, 2010; pp. 357–367. https://doi.org/10.1115/GT2010-22794.

32. Daabo, A.M.; Mahmoud, S.; Al-Dadah, R.K.; Al Jubori, A.M.; Bhar Ennil, A. Numerical analysis of small scale axial and radial turbines for solar powered Brayton cycle application. *Appl. Therm. Eng.* **2017**, *120*, 672–693. https://doi.org/10.1016/j.applthermaleng.2017.03.125.

33. Dambach, R.; Hodson, H.P. *Tip Leakage Flow: A Comparison between Small Axial and Radial Turbines*; IMechE Symposium: London, UK, 2000; pp. 1–9.

34. An Experimental Study of Tip Clearance Flow in a Radial Inflow Turbine. In *Turbo Expo: Power for Land, Sea, and Air*; ASME: Stockholm, Sweden, 1998; Volume 1. https://doi.org/10.1115/98-GT-467.

35. Serrano, J.R.; Navarro, R.; García-Cuevas, L.M.; Inhestern, L.B. Turbocharger turbine rotor tip leakage loss and mass flow model valid up to extreme off-design conditions with high blade to jet speed ratio. *Energy* **2018**, *147*, 1299–1310. https://doi.org/10.1016/j.energy.2018.01.083.

36. Tiseira, A.; García-Cuevas, L.M.; Inhestern, L.B.; Echavarría, J.D. Development of Choked Flow in Variable Nozzle Radial Turbines. *Int. J. Engine Res.* **2021**, *23*, 1388–1405. https://doi.org/10.1177/14680874211018302.

37. Serrano, J.R.; Arnau, F.J.; García-Cuevas, L.M.; Dombrovsky, A. Development and validation of a radial turbine efficiency and mass flow model at design and off-design conditions. *Energy Convers. Manag.* **2016**, *128*, 281–293. https://doi.org/10.1016/j.enconman.2016.09.032.

38. SAE Engine Power Test Code Committee. *Turbocharger Gas Stand Test Code*; SAE International: Warrendale, MI, USA, 1995. https://doi.org/10.4271/J1826_199503.

39. Serrano, J.R.; Gil, A.; Navarro, R.; Inhestern, L.B. Extremely low mass flow at high blade to jet speed ratio in variable geometry radial turbines and its influence on the flow pattern a CFD analysis. In *ASME Turbo Expo 2017: Turbomachinery Technical Conference and Exposition*; ASME: Charlotte, NC, USA, 2017; pp. 1–13. https://doi.org/10.1115/GT2017-63368.

40. Siemens. STAR-CCM + 2019.1 Release Version 14.02.010-R8. 2019. Available online: https://getintopc.com/softwares/simulators/siemens-star-ccm-2019-free-download/ (accessed on 1 September 2022).

41. Menter, F.R. Two-equation eddy-viscosity turbulence models for engineering applications. *AIAA J.* **1994**, *32*, 1598–1605. https://doi.org/10.2514/3.12149.

42. Menter, F.R.; Langtry, R.; Hansen, T. CFD simulation of turbomachinery flows—Verfication, validation and modelling. In Proceedings of the ECCOMAS 2004—European Congress on Computational Methods in Applied Sciences and Engineering, Jyväskylä, Finland, 24–28 July 2004; pp. 1–14.

43. Simpson, A.T.; Spence, S.W.T.; Watterson, J.K. A Comparison of the Flow Structures and Losses Within Vaned and Vaneless Stators for Radial Turbines. *J. Turbomach.* **2009**, *131*, 1–15. https://doi.org/10.1115/1.2988493.

44. Galindo, J.; Fajardo, P.; Navarro, R.; García-Cuevas, L.M. Characterization of a radial turbocharger turbine in pulsating flow by means of CFD and its application to engine modeling. *Appl. Energy* **2013**, *103*, 116–127. https://doi.org/10.1016/j.apenergy.2012.09.013.

45. Xue, Y.; Yang, M.; Pan, L.; Deng, K.; Wu, X.; Wang, C. Gasdynamic behaviours of a radial turbine with pulsating incoming flow. *Energy* **2021**, *218*, 119523. https://doi.org/10.1016/j.energy.2020.119523.

46. Galindo, J.; Serrano, J.R.; García-Cuevas, L.M.; Medina, N. Twin-entry turbine losses: An analysis using CFD data. *Int. J. Engine Res.* **2021**, *23*, 1180–1200. https://doi.org/10.1177/14680874211007647.

47. Zhao, B.; Qi, M.; Sun, H.; Shi, X.; Ma, C. A comprehensive analysis on the structure of groove-induced shock waves in a linear turbine. *Aerosp. Sci. Technol.* **2019**, *87*, 331–339. https://doi.org/10.1016/j.ast.2019.02.036.

48. Ananthakrishnan, K.; Govardhan, M. Influence of fillet shapes on secondary flow field in a transonic axial flow turbine stage. *Aerosp. Sci. Technol.* **2018**, *82–83*, 425–437. https://doi.org/10.1016/j.ast.2018.08.040.

49. Paniagua, G.; Yasa, T.; De La Loma, A.; Castillon, L.; Coton, T. Unsteady strong shock interactions in a transonic turbine: Experimental and numerical analysis. *J. Propuls. Power* **2008**, *24*, 722–731. https://doi.org/10.2514/1.34774.

50. Roache, P.J. Perspective: A Method for Uniform Reporting of Grid Refinement Studies. *J. Fluids Eng.* **1994**, *116*, 405–413. https://doi.org/10.1115/1.2910291.

51. Serrano, J.R.; Arnau, F.J.; De la Morena, J.; Gómez-vilanova, A.; Guilain, S.; Batard, S. A methodology to calibrate gas-dynamic models of turbocharged petrol engines with variable geometry turbines and with focus on dynamics prediction during tip-in load transient tests. In Proceedings of the ASME Turbo Expo 2020: Turbomachinery Technical Conference and Exposition, Online, 21–25 September 2020; pp. 1–14. https://doi.org/10.1115/GT2020-15169.

52. Serrano, J.R.; Tiseira, A.; García-Cuevas, L.M.; Inhestern, L.B.; Tartoussi, H. Radial turbine performance measurement under extreme off-design conditions. *Energy* **2017**, *125*, 72–84. https://doi.org/10.1016/j.energy.2017.02.118.

53. Galindo, J.; Tiseira, A.; Navarro, R.; López, M.A. Influence of tip clearance on flow behavior and noise generation of centrifugal compressors in near-surge conditions. *Int. J. Heat Fluid Flow* **2015**, *52*, 129–139. https://doi.org/10.1016/j.ijheatfluidflow.2014.12.004.

54. Deng, Q.; Niu, J.; Feng, Z. Tip leakage flow in radial inflow rotor of a microturbine with varying blade-shroud clearance. In Proceedings of the Turbo Expo: Power for Land, Sea, and Air, Montreal, QC, Canada, 14–17 May 2007; Volume 6: Turbo Expo 2007, Parts A and B, pp. 1081–1088. https://doi.org/10.1115/GT2007-27722.

55. Dambach, R.; Hodson, H.P. Tip Leakage Flow in a Radial Inflow Turbine with Varying Gap Height. *J. Propuls. Power* **2001**, *17*, 644–650. https://doi.org/10.2514/2.5791.

56. Deng, Q.; Niu, J.; Feng, Z. Study on leakage flow characteristics of radial inflow turbines at rotor tip clearance. *Sci. China Ser. E Technol. Sci.* **2008**, *51*, 1125–1136. https://doi.org/10.1007/s11431-008-0164-z.

57. Xue, Y.; Yang, M.; Martinez-Botas, R.F.; Romagnoli, A.; Deng, K. Loss analysis of a mix-flow turbine with nozzled twin-entry volute at different admissions. *Energy* **2019**, *166*, 775–788. https://doi.org/10.1016/J.ENERGY.2018.10.075.

58. A Numerical Investigation on a New Pulse-Optimized Flow Control Method for Turbocharger Turbine Performance Improvement Under Pulsating Conditions. In *Turbo Expo: Power for Land, Sea, and Air*; ASME: Montréal, QC, Canada, 2015; Volume 2C. https://doi.org/10.1115/GT2015-42059.

59. Denton, J.D. Loss mechanisms in turbomachines. *J. Turbomach.* **1993**, *115*, 621–656. https://doi.org/10.1115/1.2929299.

60. Tiseira, A.; Garcia-Cuevas, L.M.; Inhestern, L.B.; Echavarría Olaya, J.D. Numerical simulation of a radial turbine at off desing conditions in presence of choked flow. In Proceedings of the ASME Turbo Expo 2020: Turbomachinery Technical Conference and Exposition, Online, 21–25 September 2020; Volume 2E: Turbomachinery, pp. 1–14.

61. Ziaja, K.; Post, P.; Sembritzky, M.; Schramm, A.; Willers, O.; Kunte, H.; Seume, J.; di Mare, F. Numerical Investigation of a Partially Loaded Supersonic ORC Turbine Stage. In Proceedings of the ASME Turbo Expo 2020: Turbomachinery Technical Conference and Exposition, Online, 21–25 September 2020; Volume 9: Oil and Gas Applications; Organic Rankine Cycle Power Systems; Steam Turbine. https://doi.org/10.1115/GT2020-15219.

62. Zhang, L.; Zhuge, W.; Zhang, Y.; Chen, T. Similarity Theory Based Radial Turbine Performance and Loss Mechanism Comparison between R245fa and Air for Heavy-Duty Diesel Engine Organic Rankine Cycles. *Entropy* **2017**, *19*, 25. https://doi.org/10.3390/e19010025.

63. Moore, J.; Moore, J.G. Entropy Production Rates From Viscous Flow Calculations: Part I— A Turbulent Boundary Layer Flow. In Proceedings of the ASME 1983 International Gas Turbine Conference and Exhibit, Phoenix, AZ, USA. 27–31 March 1983; Volume 1: Turbomachinery. https://doi.org/10.1115/83-GT-70.

64. Kline, J.F.; Moffitt, T.P.; Stabe, R.G. *Incidence Loss for Fan Turbine Rotor Blade in Two-Dimensional Cascade*; NASA Lewis Research Center: Cleveland, OH, USA, 1983; pp. 1–12.